EES Catalysis

REVIEW ARTICLE

View Article Online
View Journal

Cite this: DOI: 10.1039/d6ey00080k

Near-infrared driven semiconductor-based photocatalysis for energy and environmental applications: mechanisms, materials, and devices

Zhiqing Wang,[a] Fangyuan Wan,[a] Yifei Wang,[a] Shengjie Bai,[a] Bin Cao,[b] Feng Wang *[a] and Ya Liu *[a]

Received 17th April 2026,
Accepted 25th April 2026

DOI: 10.1039/d6ey00080k

rsc.li/eescatalysis

Solar-driven semiconductor-based photocatalysis for fuel production and environmental protection has emerged as a promising approach to alleviate the global energy and environmental crises. Among the components of solar radiation, near-infrared (NIR) light accounts for a large portion of the spectrum and possesses unique photothermal properties, making its efficient utilization crucial for enhancing photocatalytic energy conversion. This review summarizes the mechanisms for NIR light absorption, including direct NIR absorption, photon upconversion, and plasmon-induced processes, together with representative NIR-responsive materials for CO_2 reduction, hydrogen evolution, and pollutant degradation. Recent developments in devices are also reviewed, with emphasis on the special requirements of NIR light for reactor design. Conventional performance evaluation metrics and their limitations in NIR photocatalysis have also been highlighted. Furthermore, this review also addresses current challenges and potential research directions to improve photocatalytic performance and facilitate the practical applications of NIR photocatalytic systems in energy and environmental fields.

Broader context

Solar-driven photocatalysis has long been regarded as a sustainable strategy for addressing the intertwined challenges of energy shortage and environmental pollution. However, despite decades of progress, the inefficient utilization of the near-infrared (NIR) region, accounting for nearly half of the solar spectrum, remains a fundamental bottleneck limiting overall solar-to-chemical conversion efficiency. This review highlights recent advances in mechanisms, material design, and device integration that enable effective NIR harvesting through direct bandgap engineering, plasmonic excitation, photon upconversion, and photothermal coupling. By systematically connecting light and matter interaction mechanisms with catalytic function and reactor-level optimization, this work underscores a paradigm shift from narrow-spectrum photocatalysis toward full-spectrum solar utilization. Importantly, it also addresses the need for standardized evaluation protocols to decouple photonic and thermal contributions under NIR irradiation. These advances collectively contribute to improving hydrogen evolution, CO_2 reduction, and pollutant degradation efficiencies, offering new opportunities for scalable solar fuel production and environmental remediation. The integration of NIR-responsive materials with rational device engineering provides a promising pathway toward high-efficiency, real-world solar energy conversion technologies.

1. Introduction

Energy shortage and environmental pollution resulting from human activities pose significant threats to human survival and societal sustainability.[1–3] To mitigate these challenges, it is imperative to develop strategies for reducing fossil fuel consumption and alleviating the environmental crisis. Environmentally friendly, renewable, and clean energy sources, particularly solar energy, are widely regarded as viable alternatives to fossil fuels.[4–7] Photocatalysis, which utilizes solar energy to drive oxidation and reduction reactions, has attracted significant attention for applications in the carbon dioxide reduction reaction (CO_2RR), the hydrogen evolution reaction (HER), organic degradation, and water purification.[8–12] The conversion of solar energy into chemical energy in fuels (such as H_2, CH_4, and C_2H_5OH) and its role in environmental remediation make photocatalysis an effective solution to the global energy crisis and environmental challenges.[13,14] However, its large-scale application is restricted by low conversion efficiency, poor selectivity, and unclear catalytic mechanisms.[15–19] Given that light absorption is the primary

[a] International Research Center for Renewable Energy, State Key Laboratory of Multiphase Flow, Xi'an Jiaotong University, Xi'an, Shaanxi 710049, China. E-mail: f_wang@xjtu.edu.cn, yaliu0112@xjtu.edu.cn
[b] Inner Mongolia Daqingshan Laboratory Co., Ltd, Hohhot 010020, China

step in photocatalysis, and determines the generation of electron–hole pairs, enhancing the light absorption capacity of photocatalysts is a critical strategy to improve the utilization and conversion efficiency of solar energy.

The solar spectrum consists of ultraviolet (UV) (250–400 nm), visible (vis) (400–700 nm), and near-infrared (NIR) (700–2500 nm), accounting for about 5%, 45%, and 50% of the total solar radiation, respectively. The longer the wavelength, the lower the energy of the photon. Most photocatalysts can only utilize UV or visible light; the abundant low-energy NIR photons are largely wasted. For example, TiO_2 with a large bandgap (3.2 eV) can be excited only by ultraviolet light.[20–24] The pristine graphitic carbon nitride (g-C_3N_4) can only capture light whose wavelength is less than 460 nm.[25–27] Beyond its large proportion in the spectrum, NIR light has a stronger penetration depth and a unique photothermal effect.[28–33] The photothermal effect can accelerate the reaction, increase the catalytic activity, and regulate the reaction pathways.[34–41] Thus, the effective utilization of NIR light, which accounts for approximately half of the spectral energy, is of great research significance for improving the efficiency of the overall photocatalytic system.

At present, the research on the utilization of NIR in photocatalysis focuses on two aspects: optimizing photocatalysts to extend their absorption into the NIR region; developing device configuration and integrated system design to improve mass transfer, coordinate light and thermal field management, and incorporate multiple functional modules for more efficient NIR light utilization. Wang's group anchored Ru single atoms (SAs) and nanoparticles (NPs) onto poly(heptazine imide) (PHI), respectively, *via* the in-plane Ru–N_4 coordination and interfacial Ru–N bonds, constructing a catalyst (Ru NPs/Ru-PHI) for full-spectrum photocatalytic CO_2 reduction.[42] The anchored Ru SAs introduce impurity levels in PHI, achieving NIR light absorption, while the Ru NPs facilitate the adsorption and activation of reactants and the desorption of products. Furthermore, a built-in electric field is formed between the Ru NPs and Ru-PHI, promoting the separation and migration of charge carriers. Under light irradiation ($\lambda \geq 400$ nm), this catalyst exhibited efficient CO production (32.8 μmol h^{-1}) and H_2O_2 production (23.27 μmol h^{-1}), with a high apparent quantum yield of 0.26% at 808 nm. To make full use of low-energy photons, Reisner *et al.* constructed a hybrid device integrating a photocatalyst with a solar steam generator for spectral splitting utilization.[43] In this device, the upper photocatalyst layer absorbed UV light to drive water splitting, whereas the lower solar steam generator harvested vis and NIR light to generate steam, supplying it to water-splitting reaction. The remaining water vapor was then condensed and collected as purified water. As a bifunctional system for photocatalytic hydrogen production and water purification, it achieved an STH efficiency of 0.13 ± 0.03% and an evaporation rate of about 0.95 kg m^{-2} h^{-1}. These representative advances highlight the dual approach of material innovation and system integration in NIR photocatalysis, underscoring the pivotal role of NIR light utilization in enhancing photocatalytic efficiency and improving solar energy conversion efficiency.

Despite the progress made, NIR photocatalysis still faces critical challenges, including low photocatalytic efficiency, rapid photocatalyst deactivation, unclear reaction mechanisms,

Zhiqing Wang

Zhiqing Wang is currently pursuing her PhD degree under the supervision of Prof. Liejin Guo at the State Key Laboratory of Multiphase Flow in Power Engineering, Xi'an Jiaotong University. She received her BE degree from North China Electric Power University in 2023. Her research focuses on sustainable energy conversion, specifically photocatalytic and photothermal catalytic CO_2 reduction.

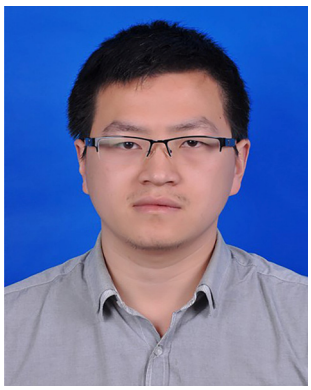

Feng Wang

Feng Wang received his PhD degree from Xi'an Jiaotong University in 2024 under the supervision of Prof. Liejin Guo. His research interests focus on designing and fabricating novel photoelectrodes/catalysts with high selectivity and high stability for photocatalytic/electrochemical CO_2 reduction.

Ya Liu

Ya Liu received his PhD degree from Xi'an Jiaotong University in 2018 under the supervision of Prof. Liang Zhao. Currently, he is an assistant professor at Xi'an Jiaotong University. From 2015 to 2016, he was a visiting scholar at Lawrence Berkeley National Laboratory under the supervision of Dr Joel Ager. His research interests focus on the development of new materials and test-bed prototypes based on abundant elements for solar fuel production.

and complex material synthesis. Realizing efficient NIR photocatalysis and practical applications requires not only the design of NIR-responsive materials but also the optimization of devices and integrated systems. However, most recent reviews on NIR light utilization have mainly focused on NIR absorption mechanisms, material design, and photocatalytic applications, with much less attention given to device and integrated system design. In this review, we summarize not only the mechanisms and representative materials for NIR light utilization and their applications in the CO_2RR, HER, and pollutant degradation but also discuss recent progress in device design and development, covering different laboratory-scale reactor configurations, large-scale devices, and integrated systems. The specific requirements that NIR light places on device design are highlighted. We also examine the applicability and limitations of conventional photocatalytic performance metrics in NIR systems, with a focus on the decoupling of photonic and thermal effects and on the need for a standardized evaluation framework. The main challenges and perspectives in NIR photocatalysis are also outlined. Overall, this review provides a systematic overview of recent developments in NIR photocatalysis, from light absorption mechanisms, material design, to device development and performance evaluation, offering a reference for future studies in photocatalysts, reactors, and system design.

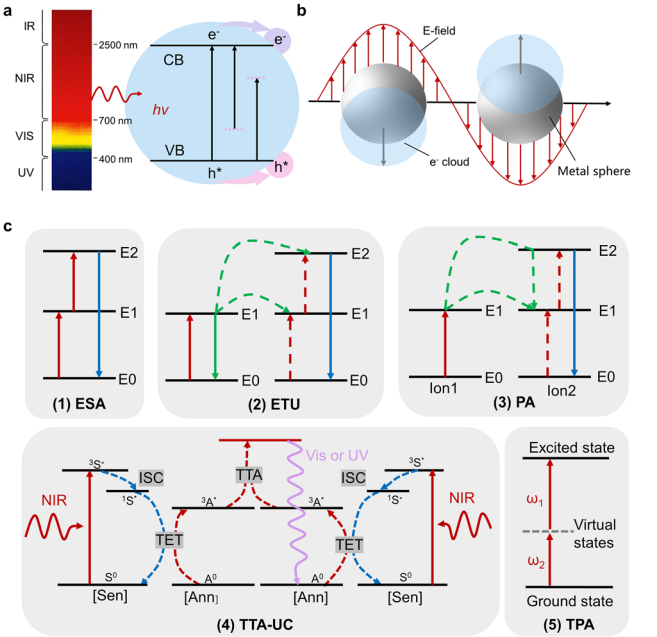

Fig. 1 (a) The principle of direct absorption of NIR light by photocatalytic materials (e^- is electron and h^+ means hole). (b) Schematic of plasma exciton oscillations on a plasma metal sphere. (c) Schematic illustration of photon upconversion mechanisms.

2. Mechanism of near-infrared light absorption

In recent years, increasing attention has been paid to the design of NIR-responsive photocatalysts to more efficiently utilize the full spectrum of solar energy.[44–48] Accordingly, it is essential to gain insight into the NIR light absorption mechanism for advancing NIR photocatalysis. Based on previous research, the mechanisms enabling photocatalysts to capture low-energy NIR photons can be broadly categorized into three types: (1) direct absorption *via* the band structure characteristics of the photocatalyst itself; (2) photon upconversion, in which long-wavelength sunlight is converted into short-wavelength light that is more readily captured; (3) the Localized surface plasmon resonance (LSPR) effect, which enhances light harvesting and facilitates the conversion of low-energy NIR photons into thermal energy.[49,50] The following sections provide a detailed discussion of each mechanism.

2.1. Direct absorption

The fundamental principle behind semiconductor absorption of solar energy lies in the compatibility between their energy band structures and the photon energies present in sunlight. When sunlight irradiates a semiconductor, photons with energies equal to or greater than the bandgap energy (E_g) can excite electrons from the valence band (VB) to the conduction band (CB). Meanwhile, excited electrons accumulate in the CB while holes are left in the VB, both of which trigger the photocatalytic reactions. Therefore, the process in which the photocatalyst directly converts NIR light into electron–hole pairs, due to its band structure, can be regarded as the direct absorption mechanism of NIR light (Fig. 1a).

For low-energy NIR photons, effective absorption and excitation of photogenerated carriers can occur only when the E_g of the semiconductor is small enough, *i.e.*, the energy band is sufficiently narrow. According to the wavelength range of NIR light (700–2500 nm), direct excitation by a single NIR photon requires the semiconductor to possess a bandgap smaller than 1.78 eV. However, this condition is difficult to satisfy for most semiconductors, except for a few intrinsically narrow-bandgap materials. To enable direct absorption of NIR light in semiconductors, two primary strategies are employed: band engineering and integration with photosensitizers. The former involves reducing the bandgap by adjusting the position of the CB or VB, or constructing intermediate energy levels within the band, dividing a wide bandgap into multiple narrower subgaps. This allows for multi-step photon excitation, enabling the harvesting of NIR photons for photocatalytic reactions. The latter can be directly excited by NIR light and subsequently transfer excited charges to semiconductors to drive the catalytic process. In both approaches, whether by modifying the intrinsic structure of the photocatalyst or by integrating it with photosensitizers, NIR light can be directly harnessed to generate charge carriers.

2.2. Localized surface plasmon resonance effect

Unlike direct absorption governed by the band structure, the LSPR effect exhibited by metal nanostructures achieves the utilization of NIR light *via* electromagnetic fields and thermal effects. LSPR is a nanoscale optical phenomenon that occurs

when the frequency of incident light aligns with the collective oscillation frequency of free electrons on the surfaces of metal nanostructures, as shown in Fig. 1b.[51,52]

The excited electrons within the metal nanostructures can decay *via* two distinct pathways. In the radiative pathway, the energy is released through the emission of photons. In contrast, the non-radiative pathway involves inelastic collisions between electrons and the recombination of electron–hole pairs. Notably, when the plasmonic energy dissipates non-radiatively, it results in the generation of hot carriers with high energy, similar to the Landau damping phenomenon.[53] Once sufficiently energized, these carriers can overcome the potential barrier at the nanoparticle boundaries and transfer to adjacent surface-adsorbed materials or semiconductors, thereby initiating ultrafast surface chemical reactions on a femtosecond timescale. Conversely, carriers that do not participate in surface reactions convert into phonons through inelastic collisions with the metal lattice. This interaction precipitates a rapid temperature increase in the lattice on a picosecond timescale. Subsequently, the accumulated thermal energy dissipates into the surrounding medium on a nanosecond timescale, driven by the interconversion of photonic and phononic energy. This energy transfer not only facilitates mass transfer but also thermodynamically promotes the chemical reaction kinetics.[50,54–56] In essence, the LSPR is associated with three concurrent effects: enhancement of the local electric field, generation of high-energy hot carriers, and induction of local heating effects. The intensified electromagnetic field promotes the photon response of nearby semiconductors, while the hot carriers produced through non-radiative decay can be directly injected into the semiconductors to participate in reactions. The photothermal effects can further convert the unused energy into heat, thereby increasing the local temperature and facilitating the reaction kinetics. However, NIR catalysis induced by the LSPR effect is not governed by a single process. In most cases, it arises from the combined contributions of local field enhancement, hot carriers, and photothermal effects, making the true dominant mechanism difficult to distinguish clearly.

2.3. Photon upconversion

It is well known that Stokes' law describes how materials typically capture high-energy (short wavelength, high frequency) light and emit low-energy (long wavelength, low frequency) light. In contrast, upconversion luminescence (UPCL) is characterized by anti-Stokes emission, which defies this convention. It involves the material being excited by low-energy light, which excites the material to emit high-energy light.[57,58] UPCL materials typically contain transition metal (d-block) or inner transition metal (f-block) elements, which enable this distinctive photoluminescent behavior.[59]

As illustrated in Fig. 1c, photon upconversion occurs *via* several fundamental mechanisms. (1) Excited state absorption (ESA): in the ESA process, a single ion sequentially absorbs multiple photons, transitioning stepwise from the ground state to higher excited states. An ion first absorbs a photon (ϕ1) to reach an intermediate metastable state (E1) and subsequently absorbs another photon resonant with the E1–E2 gap to reach a higher excited state (E2). Upon sufficient population in these upper states, radiative relaxation yields upconverted emission at shorter wavelengths.[35,60] (2) Energy transfer upconversion (ETU): ET is a process mediated by ion interactions, occurring either within the same ion or between different species. It includes several pathways: (a) successive energy transfer (SET) typically occurs between different ion species, wherein an excited donor ion transfers energy to a ground state acceptor, enabling it to an excited state. The donor relaxes to its ground state, while the acceptor may absorb a second energy transfer, reaching a higher excited level and enabling upconversion. (b) Cooperative sensitization upconversion (CSU): where two excited ions simultaneously transfer energy to a third ion, populating a higher excited state without intermediate emission. (c) Cross relaxation (CR), where two excited ions exchange energy non-radiatively, one ascending and one descending in energy. (3) Photon avalanche (PA): PA is a positive feedback excitation mechanism combining ESA and CR, with high nonlinearity and strong threshold dependence. It was initially observed in Pr^{3+}-based quantum counters. Unlike same-species ions, PA requires only a single pump beam to resonate with one transition, making it a high-efficiency UPCL process.[35,60,61] (4) Triplet-to-triplet annihilation upconversion (TTA-UC): unlike the previous three processes, which are induced by rare earth ions, TTA-UC usually occurs in organic molecular systems. The organic chromophores involved in upconversion consist of sensitizers (donors) and annihilators (acceptors). Similar to sensitizer ions in Ln^{3+} doped upconversion materials, sensitizers in TTA-UC exhibit improved light absorption in the NIR region. After absorbing a photon, the sensitizer generates a singlet excited state $[^1S]^*$, which then undergoes intersystem crossing (ISC) to the long-lived triplet excited state $[^3S]^*$. Subsequently, the energy of $[^3S]^*$ is transferred to the annihilator *via* triplet energy transfer (TET), forming a triplet annihilator $[^3A]^*$. The two $[^3A]^*$ annihilators undergo triplet fusion to form a higher energy singlet annihilator $[^1A]^*$, which emits short-wavelength light upon relaxation. The successful realization of TTA-UC has strict requirements for the relative position of the energy states of the sensitizer and annihilator. First, the energy of $[^1A]^*$ is higher than that of $[^1S]^*$, and the energy of $[^3S]^*$ is higher than that of $[^3A]^*$. In addition, the energy of $[^1A]^*$ must be lower than twice $[^3A]^*$($2[^3A]^* > [^1A]^* > [^1S]^* > [^3S]^* > [^3A]^*$).[61,62] (5) Two-photon absorption (TPA): in the TPA process, a chromophore simultaneously harvests two low energy photons within an ultrashort time through a virtual state, populating a real excited state that was originally excited by a high energy photon. By undergoing internal conversion, electron or energy transfer, the excited-state molecules are able to participate in NIR photocatalysis.[63–66]

Despite the different pathways, these upconversion mechanisms all aim to transform NIR light that is hard to utilize into more readily harvested higher-energy excitation. Upconversion is essentially a multistep energy conversion process. The efficiency of the NIR photocatalysis mediated by it is related to the upconversion efficiency, spectral matching, and interfacial energy transfer efficiency.

These three main mechanisms for NIR light utilization in current NIR photocatalysis differ clearly in both energy-conversion pathway and modes of action. Direct absorption relies on the band structure of the material itself to directly capture NIR photons, making it the most straightforward route. Photon upconversion enables the indirect use of NIR light by converting low-energy photons into higher-energy photons. In contrast, LSPR utilizes NIR light through the combined effects of local electromagnetic fields, hot carriers, and photothermal effects, and is therefore characterized by the coupling of multiple processes. Overall, these three mechanisms provide different routes for the photocatalytic conversion of NIR photons.

3. Near-infrared responsive photocatalysts

Based on the NIR light absorption mechanisms discussed above, the NIR-responsive photocatalysts can be roughly categorized into two types: direct and indirect NIR-responsive photocatalysts. The former refers to materials that can harvest NIR light spontaneously and directly convert low-energy photons into charge carriers, including intrinsic narrow-bandgap semiconductors, band-structure-regulated semiconductors, and photosensitizers. In contrast, the indirect NIR-responsive photocatalysts convert the low-energy NIR photons into high-energy photons, hot carriers, or thermal energy through UPCL and LSPR excitation to drive redox reactions. Fig. 2 illustrates the light absorption range of some representative materials with different NIR light absorption mechanisms. Extensive efforts have been made to develop NIR-responsive photocatalysts across diverse photocatalytic domains. Table 1 summarizes the advanced NIR-responsive photocatalysts in various applications, including the HER, CO_2RR, and pollutant degradation.

3.1. Direct near-infrared responsive materials

The low-energy photon capture capacity of direct NIR-responsive materials is attributed to their narrow bandgap properties. A material with a naturally narrow bandgap but free of impurities and lattice defects can be regarded as an intrinsic narrow-bandgap semiconductor. But the narrow bandgap is not always inherent. Through band structure engineering and photosensitizer modification, extrinsic semiconductors can also achieve reduced bandgaps and NIR light absorption. Of these two approaches, the former involves regulating the bandgap by inducing impurities or defects, while the latter entails combining semiconductors with NIR harvest photosensitizers.

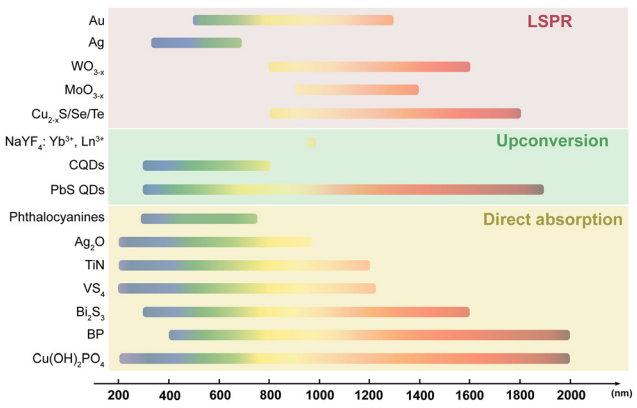

Fig. 2 The light absorption range of NIR-light responsive materials.

3.1.1. Intrinsic narrow-bandgap semiconductor. The bandgap energy determines the light absorption capacity of a semiconductor. If photon energy exceeds the bandgap, photons can be harvested by the semiconductor. Therefore, the semiconductors with narrow bandgaps are the primary choices for the NIR photocatalysts. For semiconductors that can directly capture NIR photons, the bandgap should be less than 1.78 eV, which is quite low compared to the visible or UV light-responsive materials.

The reported intrinsic narrow-bandgap semiconductors that can absorb NIR light include $Cu_2(OH)PO_4$,[67] black phosphorus (BP),[68–70] Co_3O_4,[71] some metal sulfides (Ag_2S,[72] W_2S,[73] and Bi_2S_3[74]), *etc.* Among them, the absorption band edge of narrow-bandgap sulfides is generally around 800 to 900 nm. The bandgap of BP can be changed from 0.35 to 2 eV by varying the BP layers, covering the light absorption range from vis to NIR. $Cu_2(OH)PO_4$ also exhibits a strong absorption peak in the NIR region with an absorption edge around 2000 nm. The smaller the bandgap, the wider the solar spectrum utilization range of the semiconductor. Beyond that, some transition metal catalysts have been revealed to harvest long-wavelength light due to the intraband and interband electron transition.[75–77] Feng *et al.* employed an ultrathin basic copper sulfate ($Cu_4(SO_4)(OH)_6$) nanosheet (Fig. 3a) as the photocatalyst, demonstrating the d–d transition-induced photocatalytic reaction under infrared light.[77] Under NIR light irradiation, the cascaded electron transfer processes based on d–d orbital transition were found. The degeneracy of d orbitals in Cu atoms generates empty d bands that lie within the bandgap, thereby contributing to the NIR light absorption. In detail, the electrons absorb NIR photons and are excited from the VB to the intermediate empty d bands. Next, these excited metastable electrons further absorb NIR photons and are excited to the CB, participating in the CO_2RR (Fig. 3b).

Similarly, Wang's group constructed an HO-Ru/TiN hybrid, which exhibited the properties of CO_2 reduction coupling with water oxidation under NIR light irradiation ($\lambda \geq 800$ nm) (Fig. 3c).[76] The TiN shows a marked optical absorption over the full spectrum. The absorption of NIR light comes from the small bandgap energy of about 1.1 eV and the intraband and interband transitions, which can be achieved with small solar energy. Overall, the lower the energy between adjacent orbitals or bands, the more conducive it is to the absorption of low-energy photons and the transition of electrons.

Additionally, the positions of the CB and VB will affect the redox capacity of photocatalysts. The more negative the VB is, the weaker the oxidation capacity is, and the more positive the CB is, the weaker the reduction capacity is. A small bandgap will decrease the redox capacity and accelerate carrier recombination.

Table 1 Summary of NIR-responsive photocatalytic systems based on different photocatalytic applications

Application	Photocatalyst	Absorption edge (nm)	Mechanism	Reaction system	Light source	Performance	Ref.
HER	$CuCrP_2S_6$	~1100	Direct absorption	H_2O, TEOA[a]	AM 1.5G NIR	9.12 mmol g^{-1} h^{-1} 0.66 mmol g^{-1} h^{-1}	78
	BP/Pt/RGO	~1200	Direct absorption	H_2O, EDTA[b]	Vis-NIR (λ > 420 nm) NIR (λ > 780 nm)	3.4 mmol g^{-1} h^{-1} 0.84 mmol g^{-1} h^{-1}	79
	MC-CN[c]	~1400	Direct absorption	H_2O, TEOA	Full spectrum	1.1 mmol g^{-1} h^{-1}	80
	$NaYF_4$:Yb/Tm @Ag_3PO_4/Ag@g-C_3N_4	N.A.[d]	Upconversion	H_2O, $C_3H_6O_3$	Vis-NIR (λ > 400 nm)	23.56 mmol g^{-1} h^{-1}	81
	m-TiO_2/Cu	N.A.	LSPR	H_2O, CH_3OH	UV LED (365 nm) +400 nm long-pass filter	17.8 mmol g^{-1} h^{-1}	82
	MoO_2–C@MoS_2/CdS	N.A.	LSPR	H_2O, $C_3H_6O_3$	AM 1.5G NIR (λ > 800 nm)	48.41 mmol g^{-1} h^{-1} 4.03 mmol g^{-1} h^{-1}	83
	$W_{18}O_{49}$/$Cd_{0.5}Zn_{0.5}S$	N.A.	LSPR	H_2O, Na_2S, Na_2SO_3	AM 1.5G	306.1 mmol g^{-1} h^{-1}	84
	$W_{18}O_{49}$/$ZnIn_2S_4$	N.A.	LSPR	H_2O, $C_3H_6O_3$	AM 1.5G	30.08 mmol g^{-1} h^{-1}	85
	BP-Au-CdS	N.A.	LSPR	H_2O, Na_2S, Na_2SO_3	AM 1.5G	10.1 mmol g^{-1} h^{-1}	86
CO_2RR	NiAl-Ru-LDH	~1200	Direct absorption	CO_2(g), TEOA, CH_3CN	NIR (λ = 1200 nm)	CO: 88.7 μmol g^{-1} h^{-1}	87
	MOF IHEP-15	~950	Direct absorption	CO_2(g), TEOA, CH_3CN	Vis-NIR (λ > 420 nm) NIR (λ > 720 nm)	CO: 570.3 μmol g^{-1} h^{-1} CO: 209.3 μmol g^{-1} h^{-1}	88
	2D Pb_3I_6 layers	~965	Direct absorption	CO_2(g), AA[e]	AM 1.5G	C_2H_4: 66.59 μmol g^{-1} h^{-1}	89
	Au SA/Au NPs-MoS_2	~1600	LSPR	CO_2(g), H_2O(l)	Vis-NIR	CH_3COOH: 26.9 μmol g^{-1} h^{-1}	90
	Au rod@CuPd	N.A.	LSPR	CO_2(g), H_2O(l)	AM 1.5G	CH_4: 0.55 mmol g^{-1} h^{-1}	91
	Ru@H-MoO_{3-x}	~1400	LSPR	CO_2(g), H_2O(l)	AM 1.5G NIR ($\lambda \geq$ 700 nm)	CH_4: 111.6 μmol g^{-1} h^{-1} CH_4: 39.0 μmol g^{-1} h^{-1}	92
Pollutant degradation	CuSe nanosheets	~1800	Direct absorption	RhB[f]	NIR (λ > 800 nm)	99.7% in 120 min	93
	$MoSe_2$@Bi_2S_3/CdS	~1400	Direct absorption	Cr^{6+} TCP[g]	Full spectrum	98.7% in 80 min 99.2% in 80 min	94
	Yb^{3+}/Tm^{3+}–In_2S_3	N.A.	Upconversion	Cr^{6+}RhB	Full spectrum	99.4% in 6 min 94.8% in 7 min	95
	Ag@PCNS/$BiVO_4$	N.A.	LSPR	CIP[h]	Vis-NIR (λ > 420 nm)	92.6% in 120 min	96

[a] TEOA: triethanolamine. [b] EDTA: ethylenediaminetetraacetic acid. [c] MC-CN: crystalline carbon nitride. [d] N.A.: not available. [e] AA: ascorbic acid. [f] RhB: rhodamine B. [g] TCP: 2,4,6-trichlorophenol. [h] CIP: ciprofloxacin.

Therefore, an appropriate band structure is essential for narrow bandgap semiconductors to strike a balance between light-harvesting capability and redox potential in NIR photocatalysis.

3.1.2. Band structure regulated semiconductor. The number of intrinsic narrow-bandgap semiconductors is always limited, and most materials have a wide bandgap, which cannot absorb NIR light. Energy band engineering is a typical strategy for designing the band structure of traditional wide bandgap materials. By introducing impurity atoms, defects, or disorders, the electronic structure and the stoichiometry of the semiconductor can be regulated, and the light absorption can also be broadened to the NIR region.[97,98]

Doping conventional semiconductors with metal (Cu, Fe, Ni, In, Co) or non-metal (C, N, P, S) atoms is a prevalent way to design the band structure. Impurity atom doping results in the formation of impurity levels in semiconductors. The existence of the impurity level divided the process of photon-excited electron transition into two steps: electron excitation from the VB to the impurity level, and then excitation from the impurity level to the CB. Consequently, the energy required for the electron transition is greatly reduced, and low-energy infrared photons can excite the semiconductor to produce charge carriers. Su *et al.* synthesized C and K co-incorporated red polymeric carbon nitride (RPCN) through a salt-template-induced homogeneous strategy (Fig. 3e).[99] Compared with traditional PCN, the synthesized RPCN exhibits a narrower bandgap (1.71 eV) and a wider light absorption range (the light absorption edge near 1000 nm), as illustrated in Fig. 3d. Consequently, RPCN realizes a high H_2 evolution from water (140 μmol g^{-1} h^{-1}) under NIR light. The existence of disordered structures in semiconductors can also regulate the band structure.

Mao *et al.* introduced disorder to the surface of nanophase TiO_2 through hydrogenation, obtaining black TiO_2 nanocrystals.[100] The density of states (DOS) of disorder-engineered black TiO_2 and unmodified TiO_2 reveals that the VB maximum energy of black TiO_2 upshifts by about 2.18 eV, resulting in a much narrower bandgap. The solar absorption-enhanced black TiO_2 exhibited substantial photooxidation of organic molecules and hydrogen production. Moreover, D-HNb_3O_8 with disorder was constructed, achieving full spectrum (250–2500 nm) absorption.[101] The D-HNb_3O_8 monolayer includes two phases: crystalline domains and disordered nanoislands. The ordered structure of D-HNb_3O_8 captures the high-energy photons for photoexcited charge carriers to drive photo-redox reactions, while the disordered structure absorbs the full solar energy

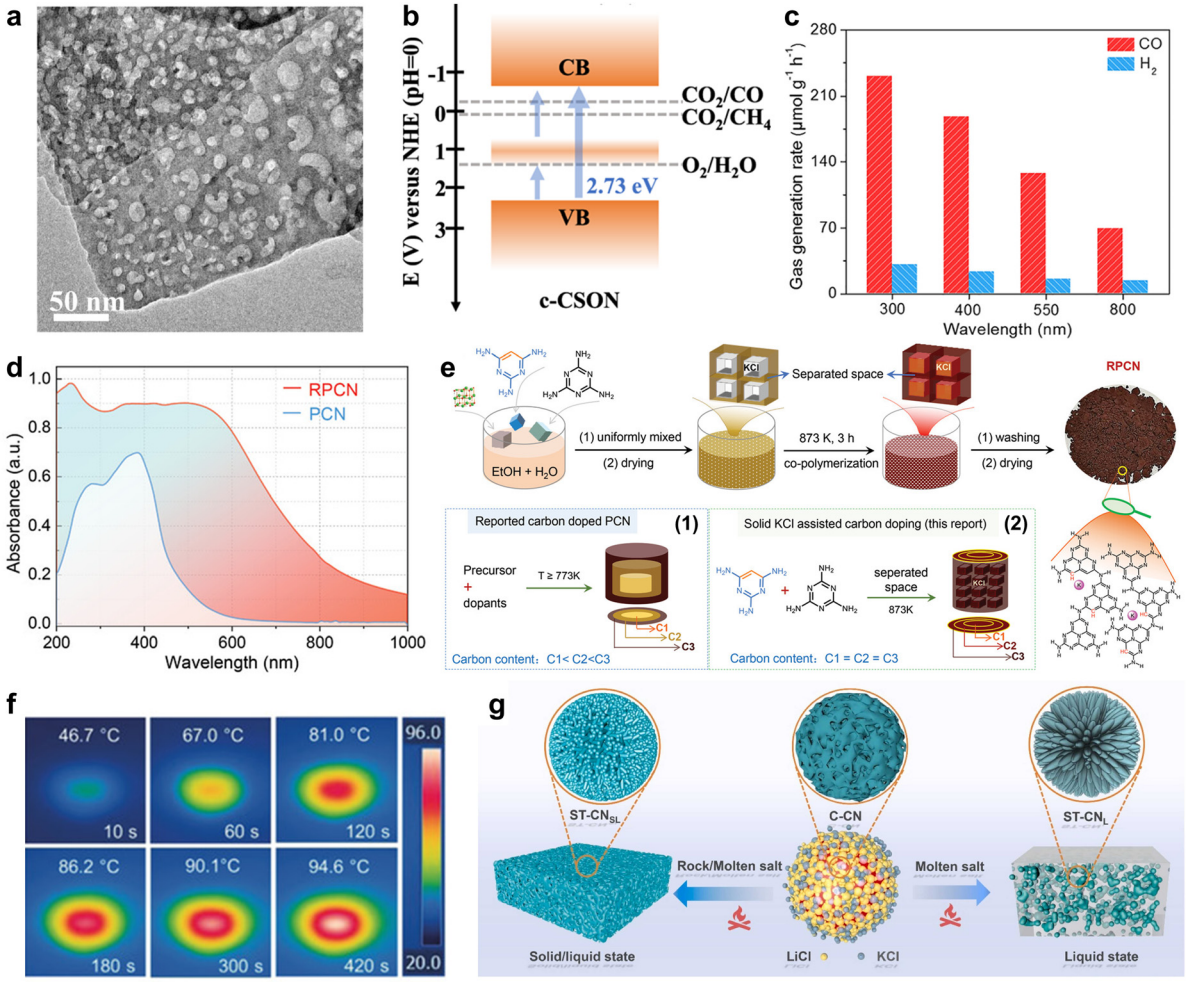

Fig. 3 (a) TEM image of $Cu_4(SO_4)(OH)_6$ nanosheets. (b) The electronic band structures of $Cu_4(SO_4)(OH)_6$. Reproduced with permission from ref. 77. Copyright 2023, Springer Nature. (c) CO_2 reduction performance of HO-Ru/TiN under different wavelengths of illumination. Reproduced with permission from ref. 76. Copyright 2023, American Chemical Society. (d) UV-vis-NIR DRS spectra of PCN and RPCN. (e) The preparation process of RPCN: (1) the comparison of reported carbon-doped PCN, and (2) the reported KCl-induced carbon/potassium co-doping process. Reproduced with permission from ref. 99. Copyright 2021, John Wiley and Sons. (f) Infrared images of D-HNb_3O_8 under simulated 1 sunlight irradiation. Reproduced with permission from ref. 101. Copyright 2018, John Wiley and Sons. (g) Illustration for the synthesis of Salt Treated-CN_X (X = SL (solid/liquid) or L (liquid)). Reproduced with permission from ref. 103. Copyright 2024, Elsevier.

and transforms it into heat to boost the reaction kinetics. Fig. 3f presents the infrared images of D-HNb_3O_8 under simulated one-sun irradiation. Compared with pristine HNb_3O_8, D-HNb_3O_8 exhibits a more pronounced temperature increase, rising from 25 °C to 95 °C within several minutes. This result suggests that the introduction of a disordered structure enhances light absorption and promotes a strong photothermal effect.

The presence of vacancies will also modulate the band structure of a material, thereby altering its optical properties. Zhang *et al.* prepared a vacancy-rich BiO_{2-x} monolayer that exhibits full-spectrum absorption capacity and enhanced photocatalytic activity for RhB and phenol removal under UV, visible, and NIR irradiation.[102] The DOS and XPS spectra demonstrate that the presence of abundant V_{Bi-O} defects decreases the bandgap to 1.46 eV with both up-shifted VB maximum and CB minimum. Besides, the increased oxygen vacancies (OVs) in monolayer BiO_{2-x} typically induced stronger light absorption. In some cases, the reduction of vacancies can also lead to enhanced light absorption. A highly crystalline C_3N_4 has been prepared through the treatment of an oxygen-containing precursor by the semi-molten-salt approach (Fig. 3g).[103] In this process, the incorporation of structural oxygen modulates the electronic structure of C_3N_4 and narrows the bandgap to 1.67 eV, extending the absorption edge toward the NIR region. Meanwhile, the semi-molten-salt treatment suppresses the formation of undesired nitrogen defects and preserves high crystallinity, thereby facilitating charge separation and migration and suppressing carrier recombination. The broadened NIR harvesting and efficient charge utilization achieve overall water splitting activity under NIR light irradiation.

By changing the position of the CB and VB, or introducing intermediate levels, band structure engineering achieves wide-

spectrum absorption while retaining a certain redox capacity. Compared with intrinsic narrow-bandgap materials, it offers more flexible regulation and a wider choice of materials, making the NIR response easier to achieve. But band structure engineering is often accompanied by more complex structural changes. Appropriate defect introduction or doping can improve light absorption and carrier separation, while excessive amounts may act as recombination centers, leading to increased non-radiative loss and reduced structural stability and photocatalytic activity.

3.1.3. Photosensitizers. In addition to the aforementioned materials, photosensitizers are another class of substances that can directly respond to NIR light. Photosensitizers absorb photons and transfer the absorbed light energy to the reactants in various forms, without undergoing any changes in mass or chemical properties before and after the chemical reaction. The definition of a photosensitizer is quite similar to that of a photocatalyst, with the key distinction being that photocatalysts can directly engage in redox reactions with the substrate, while photosensitizers transfer the excited state energy to the reactant through various pathways such as free radical initiation, redox reaction, and energy transfer. Therefore, constructing NIR-absorbing photosensitizers is a strategy for the direct utilization of low-energy NIR photons. The photoexcited electrons generated by photosensitizers can be injected into the CB of the connected semiconductor to drive the surface redox reaction. Organic dyes and metal complexes are among the most extensively investigated photosensitizers for solar light harvesting.[87,104–110]

Owing to the excellent light absorption properties and tunable molecular structures, organic dyes are widely applied in reactions such as water splitting, CO_2 reduction, and the degradation of organic pollutants, thereby enhancing the solar energy utilization efficiency of the system. A variety of organic dye photosensitizers have been developed, including porphyrins, phthalocyanines, Eosin Y, Rose Bengal, Rhodamine B, *etc.* Each dye exhibits a characteristic absorption spectrum, which is closely related to its molecular structure and functional groups.[111] A self-assembled tetrakis(4-carboxyphenyl)porphyrin (SA-TCPP) supramolecular photocatalyst has been reported to be employed in high-efficiency H_2O_2 generation.[110] This porphyrin photocatalyst exhibited broadband absorption extending to 1100 nm, with a quantum efficiency of 14.9% at 420 nm and 1.1% at 940 nm. Benefiting from the photothermal effect of NIR light, the reaction temperature reached 328 K under simulated sunlight irradiation, achieving a solar energy-to-chemical efficiency of approximately 1.2%. Similarly, phthalocyanines and their derivatives have been designed to broaden the spectral response and enhance photocatalytic performance.[105,107–109] Peng's group employed a highly asymmetric zinc phthalocyanine derivative (Zn-tri-PcNc) as a sensitizer to extend the spectral response region of g-C_3N_4.[107] Zn-tri-PcNc/g-C_3N_4 exhibited a much broader absorption band with an edge exceeding 850 nm, compared to approximately 450 nm for g-C_3N_4. The optimized Zn-tri-PcNc/g-C_3N_4 photocatalyst achieved an H_2 production rate of 125.2 μmol h^{-1} under the illumination of light ($\lambda \geq 500$ nm) and a high apparent quantum yield (AQY) of 1.85% at 700 nm with chenodeoxycholic acid (CDCA) as the co-adsorbent. In addition, Zn-tri-PcNc and naphthalocyanine (Zn-tetra-Nc) sensitized TiO_2 were constructed for H_2 evolution.[108] The similar AQY curve and DRS spectrum indicated that the light absorption property of the sensitizer determines the photocatalytic activity. However, the solar absorption range of a single photosensitizer is limited, covering only a few hundred nanometers.

Based on the previous work, Peng and co-workers carried out a co-sensitized g-C_3N_4 system with an indole-based D–π–A organic dye (LI-4) and Zn-tri-PcNc (Fig. 4a). As a result, the H_2 production activity of the co-sensitized catalyst LI-4/g-C_3N_4/Zn-tri-PcNc reached 371.4 μmol h^{-1} under irradiation of light with a wavelength greater than 500 nm, significantly outperforming the system with only a single photosensitizer.[109]

Metal complexes ($Ru(bpy)_3^{2+}$, $Ir(ppy)_3$, $Re(bpy)(CO)_3Cl$, *etc.*) form a class of photosensitizers composed of transition metal ions coordinated with organic ligands, featuring tunable electronic structures, notable visible light absorption, and long-lived excited states, and are widely applied in photocatalytic systems.[112–115] Recently, a novel photocatalyst, ruthenium-intercalated NiAl-layered double hydroxide (NiAl-Ru-LDH), was reported to achieve efficient and highly selective CO_2 reduction under NIR light illumination at a wavelength of 1200 nm, with a CO selectivity of 84.81% and a yield of 0.887 μmol h^{-1} (Fig. 4b).[87] In this study, the incorporation of the Ru metal complex into the NiAl-LDH structure significantly reduced the bandgap and broadened the light absorption into the NIR region. The Ru complex is critical in enhancing light harvesting and facilitating electron transfer, underscoring its potential for application in NIR-driven photocatalysis. Additionally, purely organic photosensitizers have also been explored to achieve efficient light absorption and photocatalytic performance under NIR light. Chou *et al.* developed a series of ITIC- and BTIC-based polymer photocatalysts, which regulate the light absorption range and photogenerated charge separation efficiency by designing the chemical structures of the PITIC-X and introducing various π-linkers (X)

between the repeating units of the polymer backbone.[116] A schematic illustration of the PBTIC-X polymers is shown in Fig. 4c and d. The constructed polymers with different π-linkers exhibited different HOMO and LUMO values, while the corresponding π-linkers are ThF < Th < Ph, from lowest to highest (Fig. 4e). Among various combinations, the PITIC-ThF polymer achieved the highest hydrogen evolution rate of 20.5 μmol h^{-1} under NIR (>780 nm) irradiation and exhibited an apparent quantum yield (AQY) of 4.76% at 700 nm (Fig. 4f). This strategy demonstrates that intramolecular π-bridge engineering is an effective approach to modulating charge behavior, broadening light absorption, and improving the overall photocatalytic performance of polymer-based systems.

Besides metal complexes and organic dyes, new photosensitizers, such as organic π-conjugated photosensitizers, have also been developed recently. Photosensitizers can effectively extend the light absorption range of photocatalysts, and their structures are flexible, making the absorption wavelength easier to

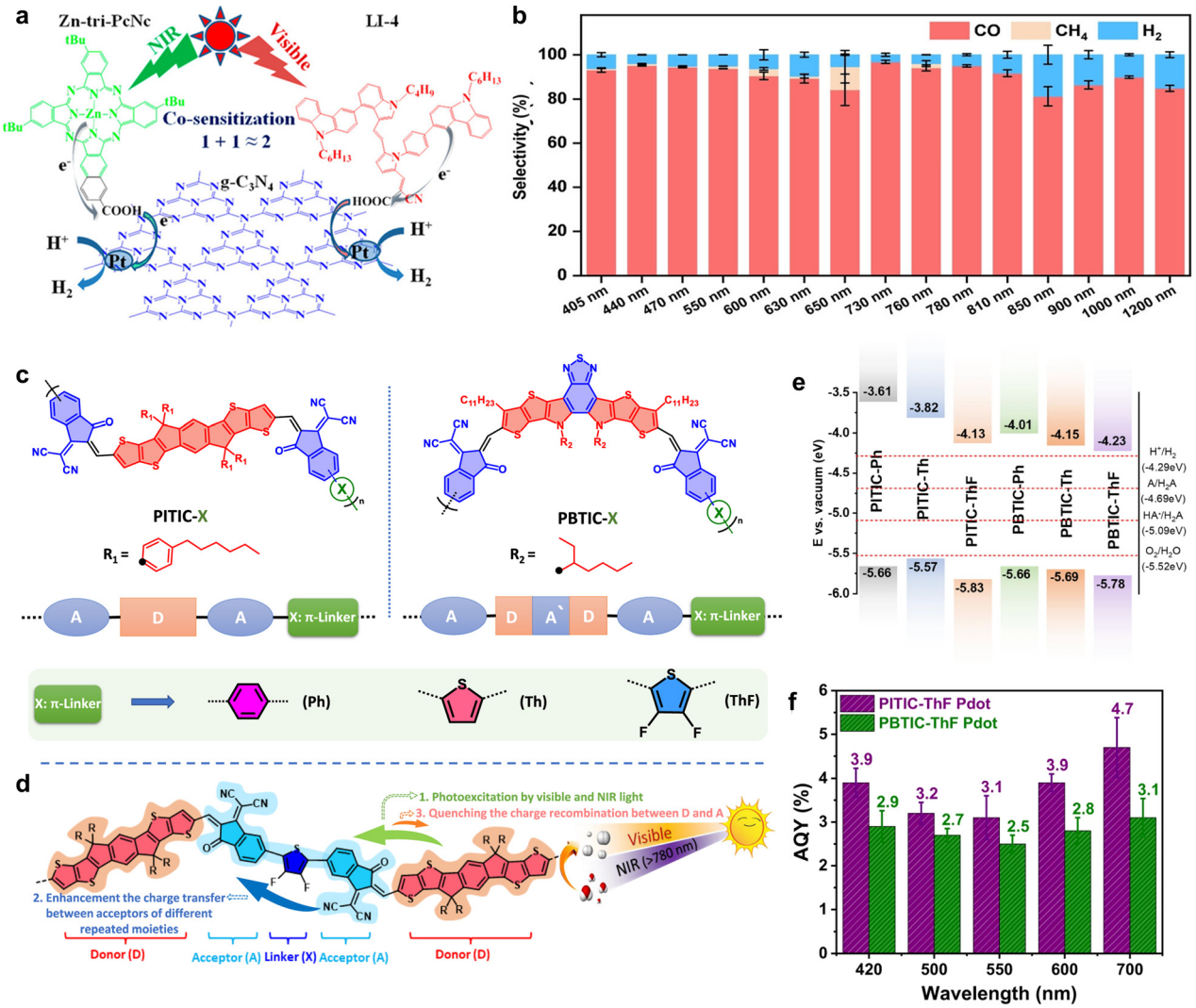

Fig. 4 (a) Proposed co-sensitization mechanism of g-C_3N_4 for photocatalytic H_2 production. Reproduced with permission from ref. 109. Copyright 2015, American Chemical Society. (b) Selectivity to CO, CH_4, and H_2 on NiAl-Ru-LDH under different wavelengths. Reproduced with permission from ref. 87. Copyright 2024, John Wiley and Sons. (c) Chemical structures of the PITIC-X and PBTIC-X polymers with various π-linker units (X = Ph, Th, and ThF). (d) Illustration of the charge transfer through the PITIC-ThF polymer chain during the photocatalytic reaction under visible and NIR light. (e) Energy level diagrams of all the polymers were determined using a photoelectron spectrometer. The dashed lines in the diagram represent the proton reduction potential (H^+/H_2), water oxidation potential (O_2/H_2O), and the calculated potential of the two-hole (A/H_2A) and one-hole (HA/H_2A) oxidation of ascorbic acid at pH 2.6 (the experimentally measured pH of a 0.1 M ascorbic acid solution). (f) The AQY for the PITIC-ThF Pdots and PBTIC-ThF Pdots under different wavelengths. Reproduced with permission from ref. 116. Copyright 2024, Springer Nature.

adjust. However, photosensitizers are often subject to photobleaching, desorption, degradation, and poor cycling stability. Moreover, the interfacial coupling efficiency between the photosensitizer and the photocatalyst directly impacts the overall performance. Once electron or energy transfer becomes insufficient, the photocatalytic activity decreases markedly. As a result, the practical application of photosensitizers is mainly restricted by material stability and interfacial transfer efficiency.

Direct NIR-responsive materials can absorb NIR light without additional energy conversion units, which simplifies the system and clarifies the underlying mechanism. However, achieving NIR absorption usually requires a narrower bandgap, which reduces the redox driving force and increases carrier recombination and non-radiative loss. Although band structure engineering and photosensitizers can help extend the absorption edge, they may also introduce more recombination centers and structural instability. Therefore, the main challenge to the direct NIR-responsive materials is not only to realize NIR absorption, but also to maintain a balance among the absorption range, carrier dynamics, redox capacity, and long-term stability.

3.2. Indirect near-infrared responsive materials

Unlike direct NIR-responsive materials that can be directly excited by NIR light to produce electron–hole pairs, indirect NIR-responsive materials involve multiple energy transfers and

conversions before participating in the photocatalytic reaction. Materials with upconversion luminescence capabilities or the LSPR effect are representative indirect NIR-responsive materials, often used in photocatalysts to improve light absorption. Specifically, upconversion materials can transform NIR light into UV or visible light, which conventional photocatalysts can absorb readily. In contrast, plasmonic materials leverage the LSPR effect to generate localized heat or hot carriers that contribute to photocatalytic activation. These energy conversion processes effectively enable the system to indirectly harvest NIR light, thereby expanding the usable portion of the solar spectrum.

3.2.1. Upconversion materials. Upconversion materials feature distinct electronic structures that enable the conversion of low-energy NIR photons into higher-energy photon emissions, offering significant potential for NIR photocatalysis.[117,118] Among them, lanthanide (Ln)-doped inorganic nanoparticles, such as $NaYF_4$ doped with Yb^{3+}/Er^{3+} or Yb^{3+}/Tm^{3+}, are the most commonly used upconversion materials. They possess well-defined ladder-like 4f energy levels and long-lived intermediate states, facilitating efficient photon upconversion through mechanisms such as ETU, ESA, *etc.*[119–122] Additionally, quantum dots (QDs) and organic molecular systems can also achieve infrared light absorption through multi-photon absorption or TTA-UC mechanisms.[123,124] The upconversion is made possible in these materials by their precise energy-level alignment and efficient non-radiative transfer. This capability allows NIR light to trigger conventional photocatalysts, thereby significantly improving solar energy utilization.

Most Ln series elements have an unfilled 4f electron shell, showing a trivalent state in the crystal. The electron transition between the 4f layers of this electronic structure provides multistate energy levels, and the excited states possess long lifetimes, up to tens of milliseconds, which makes them excellent inorganic upconversion materials.[58,125] Doping semiconductors with Ln ions can achieve upconversion emission from NIR light to vis or UV light. Ln^{3+}-doped upconversion materials mainly consist of three parts: the matrix material, the active ion, and the sensitized ion. The substrate material can provide the reaction site, while sensitized ions enhance light absorption and transfer the absorbed energy of low-energy photons to the active ions. The active ions absorb energy, transition to the highly excited state, and then return to the ground state, releasing high-energy photons to achieve UPCL. Among them, $NaYF_4$, $NaGdF_4$, and CaF_2 are the matrix materials, Er^{3+}, Tm^{3+}, and Ho^{3+} are commonly used as active ions, while Yb^{3+} is commonly used as a sensitized ion.

Different combinations of matrix, active ions, and sensitized ions can result in variations in both upconversion efficiency and emission wavelength. Ding *et al.* synthesized well-defined β-$NaYF_4$:Yb^{3+},Ln^{3+} (Ln = Er, Tm, Ho) microrods through a rapid microwave-assisted flux cooling method.[126] The photoluminescence spectra of β-$NaYF_4$:Yb^{3+},Ln^{3+} exhibited multi-color upconversion emissions for different species of dopant under 980 nm laser diode excitation. Furthermore, the concentrations of active and sensitized ions play a critical role in determining the upconversion efficiency and the emission profile. Zhao and co-workers experimentally confirmed that the UPCL of $NaYF_4$:Yb/Tm nanocrystals is significantly enhanced with the increasing Tm^{3+} content under high-irradiance excitation.[127] The upconversion emission of 8 mol% Tm^{3+} nanocrystals is 70 times stronger than that of 0.5 mol% Tm^{3+} nanocrystals at 802 nm. Similarly, increasing the Yb^{3+} doping concentration has also been shown to enhance the UPCL intensity.[128] However, excessively high doping concentrations can lead to pronounced concentration quenching, significantly reducing the quantum efficiency. Elevated dopant levels may also induce cross-relaxation processes and alter the energy level distribution, resulting in spectral shifts in the upconverted emission. Therefore, optimizing the concentrations of both sensitized and active ions is essential for balancing emission intensity, wavelength control, and energy conversion efficiency in NIR-excited upconversion systems. Due to their well-defined and tunable NIR absorption and upconversion properties, the Ln-doped materials have been broadly employed in NIR photocatalysis.[81,95,129] For example, Sung *et al.* reported a full-spectrum solar light responsive photocatalyst $NaYF_4$:Yb/Tm@Ag_3PO_4/Ag@g-C_3N_4 (Fig. 5a).[81] As illustrated in Fig. 5b, under sunlight illumination, the core $NaYF_4$:Yb/Tm harnesses the NIR photons and supplies additional UV-Vis photons *via* the UPCL process to the shell Ag_3PO_4/Ag@g-C_3N_4. In the photocatalytic HER experiment, the NIR-responsive $NaYF_4$:Yb/Tm@Ag_3PO_4/Ag@g-C_3N_4 achieved an H_2 evolution rate of 23.56 mmol g^{-1} h^{-1}, significantly outperforming the NIR-inactive photocatalyst ($NaYF_4$@Ag_3PO_4/Ag@g-C_3N_4), which only yielded 16.32 mmol g^{-1} h^{-1}. Deng's group reported a selectivity-enhanced photocatalytic system based on $NaNdF_4$ nanocrystals combined with Zn(II) phthalocyanine (ZnPc) (Fig. 5c and d).[130] The UV-vis absorption spectra and PL spectra of photocatalysts are shown in Fig. 5e. This approach utilizes the NIR absorption bands of Nd^{3+} ions (~808 nm) and enables direct energy transfer from excited Nd^{3+} to the triplet state of ZnPc *via* a lanthanide-mediated triplet sensitization pathway, achieving NIR-driven dehydrogenation and C–N coupling reactions. These results highlight the advantages of Ln-doped upconversion systems, such as their tunable emission profiles, long-lived excited states, and high photostability. However, challenges, including concentration-dependent quenching, narrow absorption bands, and low quantum yields under low-power excitation, remain critical issues that need to be addressed for practical photocatalytic applications.

Meanwhile, QDs have emerged as promising upconversion materials due to their unique size-dependent photoluminescence properties.[131–133] Typically, they are defined as zero-dimensional nanomaterials with diameters smaller than the exciton Bohr radius (generally less than 10 nm).

QDs exhibit broad spectral responsiveness and large absorption cross-sections, making them well-suited for NIR-driven photocatalysis. Among them, carbon quantum dots (CQDs) are particularly attractive owing to their low toxicity, cost-effectiveness, and favorable UPCL characteristics. CQDs display a broad and continuous excitation range and emit in the UV-vis region, which can be attributed to the photoexcitation of π-conjugated electrons within the sp^2-hybridized carbon

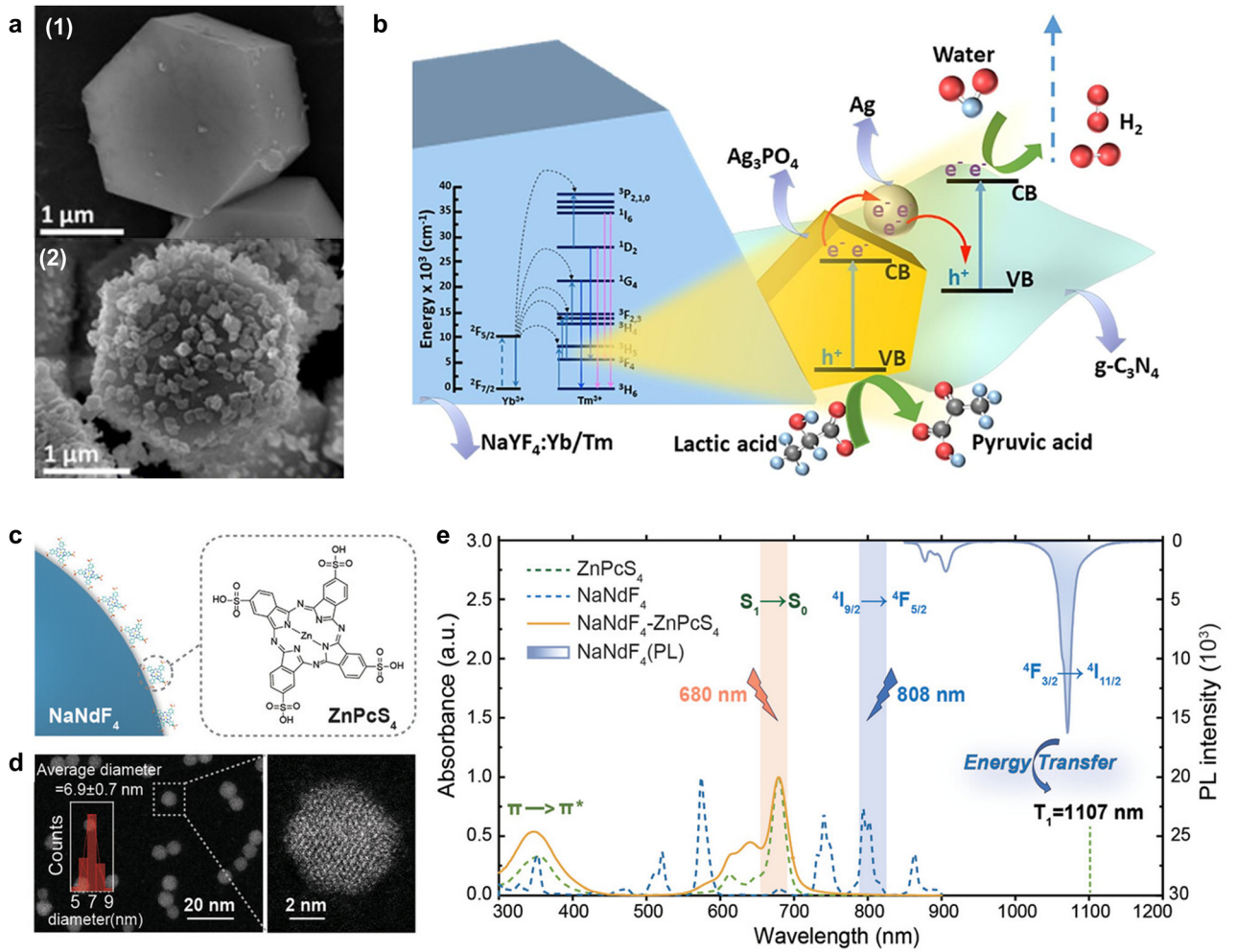

Fig. 5 (a) FE-SEM images of (1) $NaYF_4$:Yb/Tm, and (2) $NaYF_4$:Yb/Tm@Ag_3PO_4/Ag. (b) Schematic representation of the photocatalytic H_2 evolution mechanism of the $NaYF_4$:Yb/Tm@Ag_3PO_4/Ag@g-C_3N_4 photocatalyst under sunlight illumination. Reproduced with permission from ref. 81. Copyright 2021, Elsevier. (c) Schematic structure of a $NaNdF_4$–$ZnPcS_4$ nanocomposite. (d) Spherical aberration-corrected TEM image of $NaNdF_4$ nanocrystals with a histogram showing particle size distribution. (e) UV-Vis absorption spectra of $ZnPcS_4$, $NaNdF_4$, and $NaNdF_4$–$ZnPcS_4$, along with the photoluminescence (PL) spectrum of $NaNdF_4$ in DMSO solution. Reproduced with permission from ref. 130. Copyright 2025, John Wiley and Sons.

framework.[134] Li and coworkers reported the size-dependent UCPL properties of CQDs with different sizes synthesized *via* a one-step alkali-assisted electrochemical method.[135] Specifically, the small CQDs (1.2 nm) emitted UV light (about 350 nm), the medium-sized CQDs (1.5–3 nm) exhibited visible light (400–700 nm) luminescence, and the large CQDs (3.8 nm) exhibited NIR emission. Theoretical calculations revealed that the redshift in emission concomitant with increasing size is due to the gradual narrowing of the HOMO–LUMO energy gap. This tunable emission facilitates the spectral matching of CQDs with semiconductors possessing different bandgaps, extending light absorption into the NIR region and enhancing solar energy utilization.

Furthermore, UPCL has also been observed in emerging materials beyond conventional Ln-doped systems and QDs. Ji and co-workers reported an ESA-based upconversion mechanism in nitrogen-deficient g-C_3N_4 (g-C_3N_x), where abundant N_{2C} vacancies serve as intermediate states.[136] Upon 800 nm excitation, g-C_3N_x exhibits visible upconverted emission at 436 nm, attributed to defect-mediated electronic transitions. In another study, Wu *et al.* developed a TTA-UC system comprising zinc-doped and ZnS-coated $CuInSe_2$ nanocrystals (ZCISe NCs) as sensitizers, 5-tetracene carboxylic acid (TCA) as the transmitter, and rubrene as the annihilator.[137] This system displays upconversion from NIR light to yellow light with an external quantum efficiency of 16.7% and enables efficient NIR-driven organic synthesis and polymerization. With the ability to convert low-energy NIR photons into higher-energy emissions, upconversion materials can extend the light-harvesting range of photocatalysts, providing an available strategy for NIR light utilization. However, their overall performance is often limited by low conversion efficiency and multistep energy losses. Conventional Ln^{3+}-doped upconversion materials still suffer from low quantum efficiency and high excitation thresholds, while TTA-UC systems, despite lower power requirements, remain susceptible to oxygen quenching, photobleaching, and

environmental instability. In addition, spectral mismatch and light absorption competition between the upconversion material and the photocatalyst further reduce the effective utilization of NIR photons. Therefore, many current NIR photocatalytic systems based on upconversion materials remain at the laboratory research stage, rather than practical application.

3.2.2. Materials with localized surface plasmon resonance effects. The LSPR effect is a collective oscillation between the free electrons of metal nanostructures and incident photons when the frequency of incident light is in resonance with the natural oscillation frequency of surface free electrons in the metal nanostructures.[138,139] The materials with the LSPR effect, on the one hand, can generate a strong response in the NIR band through plasmon resonance. On the other hand, the strong local electric field produced by LSPR can also activate adjacent materials and enhance their light absorption capacity.

The LSPR effect mainly occurs in noble metals like Ag, Au, Pt, and Pd.[140] The absorption peak position of noble metal nanostructures can be affected by the type, shape, and size of materials, and the environment.[141–143] Typically, the LSPR absorption peaks of spherical Ag nanoparticles are between 400 and 450 nm, while that of spherical Au nanoparticles is around 500 nm.[144] With the increase in size, the LSPR absorption peak undergoes a redshift.[145] Furthermore, the shape changes of metal nanostructures can also cause changes in the peak position of LSPR. When Au is made into nanorods (NRs), the longitudinal LSPR peak can extend to the NIR region and is proportional to the aspect ratio of Au NRs.[146] Similarly, when the shape of Ag nanoparticles changes from spherical to pentagonal and to triangular geometries, the resonant wavelength red-shifts from 450 to 670 nm.[147] The scattering spectra of single Ag nanoparticles in different shapes are displayed in Fig. 6a. However, the mismatch for pure noble metals between ultrafast energy relaxation and slow chemical reduction kinetics across disparate timescales seriously hinders the conversion efficiency of solar energy. Combining noble metals with electron acceptors and semiconductors is a feasible strategy to decrease heat loss. Generally, noble metal nanoparticles act as cocatalysts in the reaction, providing broad spectral absorption. Xiong's group employs Au NRs as light harvesters and copper-palladium (CuPd) alloy shells as CO_2 adsorption and reaction active sites, constructing a plasmonic nanocatalyst for efficient CO_2RRs across the full spectrum (Fig. 6b).[91] Under 400 mW cm^{-2} full-spectrum light illumination, Au rod@$CuPd_2$ achieved nearly 100% CH_4 selectivity and a CH_4 yield of 0.55 mmol g^{-1} h^{-1}, without a sacrificial agent. The wavelength-dependent apparent quantum efficiency (AQE) of Au rod@$CuPd_2$ is up to 0.38% at 800 nm in the gas–solid system. To study the reasons for the high utilization rate of low-energy photons, the authors analyzed the projected density of states of the photocatalytic system with and without an electric field, as illustrated in Fig. 6c. In the presence of the electric field, a series of new quasi-isolated trap states emerge above the E_f, which can effectively extend the lifetime of hot electrons and increase the probability of electron re-excitation by subsequent low-energy photons.

Remarkably, the LSPR effect is also observed in transition metal oxides with OVs (WO_{3-x}, MoO_{3-x}) and copper chalcogenides ($Cu_{2-x}S$, $Cu_{2-x}Se$) due to their high carrier density.[148–155] Shi and co-workers utilized the LSPR effect of WO_{3-x} to broaden the light absorption of $Znln_2S_4$ (ZIS).[156] The pure WO_{3-x} showed a wide NIR light absorption range (800–1500 nm), and WO_{3-x}/ZIS composites exhibited strong light absorption within 730–850 nm with an increase in WO_{3-x} content. The increased local temperature caused by the LSPR effect and the interface electric field between WO_{3-x} and ZIS accelerated the reaction and promoted charge separation, thereby enabling photocatalytic H_2 production when $\lambda >$ 800 nm. Similarly, after introducing OVs into MoO_3 nanosheets, Xiao *et al.* observed strong absorption across 200–1400 nm.[92] This broad absorption was attributed to oxygen vacancy-induced plasmonic absorption, where the mixed Mo^{6+}/Mo^{5+} valence states supplied free carriers for LSPR excitation. Meanwhile, the incorporation of substituted Ru single atoms induced clear charge transfer and generated electron-rich Ru centers and electron-deficient Mo centers, which enhance charge polarization, suppress carrier recombination, and spatially separate the activation sites for H_2O and CO_2. By the synergy between oxygen vacancy and Ru atom substitution, the modified Ru@H-MoO_{3-x} photocatalyst exhibits a superior CO_2RR activity with a CH_4 evolution rate of 111.6 μmol g_{cat}^{-1} under the full spectrum. Furthermore, under NIR light irradiation, a CH_4 yield of 39.0 μmol g_{cat}^{-1} was also observed, which is attributed to the long-wavelength light absorption caused by the LSPR effect. The LSPR effect of WO_{3-x} and MoO_{3-x} is derived from the accumulation of free electrons, originating from OVs, which can resonate with the incident light. In contrast, the LSPR effect of copper chalcogenides is due to the existence of a large number of copper vacancies, thereby forming a high concentration of free holes. Yung *et al.* developed a dual-plasmonic photocatalytic system based on Au@Cu_7S_4 yolk@shell nanocrystals for efficient H_2 production across the visible to NIR spectra region.[157] The dual-plasmonic heterostructure combines plasmonic metals (Au) and plasmonic semiconductors (Cu_7S_4) to enable wide-spectrum photon capture. As illustrated in Fig. 6d, compared to pure Cu_7S_4, Au@Cu_7S_4 exhibited long-lived charge separation states under both visible and NIR excitation, prolonging the lifetime of the delocalized electrons to promote hydrogen production. Remarkably, with additional co-catalysts, this system achieves a quantum yield of 7.3% at 2200 nm, demonstrating its exceptional NIR responsiveness. In another study, a dual-plasmon resonance photocatalyst comprising Au particles and Cu_7Te_4 nanowires was employed for photothermal CO_2RR driven by infrared light (Fig. 6f).[158]

The dual LSPR effect not only enhances the absorption in the NIR region but also effectively reduces the thermodynamic reaction energy barrier, thereby promoting the selective generation of CO, as shown in Fig. 6e. Consequently, the Au–Cu_7Te_4 nanowires displayed a CO production rate of 2.7 μmol g^{-1} h^{-1} with 100% selectivity for atmospheric CO_2 reduction under infrared light irradiation (Fig. 6g). Materials exhibiting the LSPR effect are attractive for their capacity to

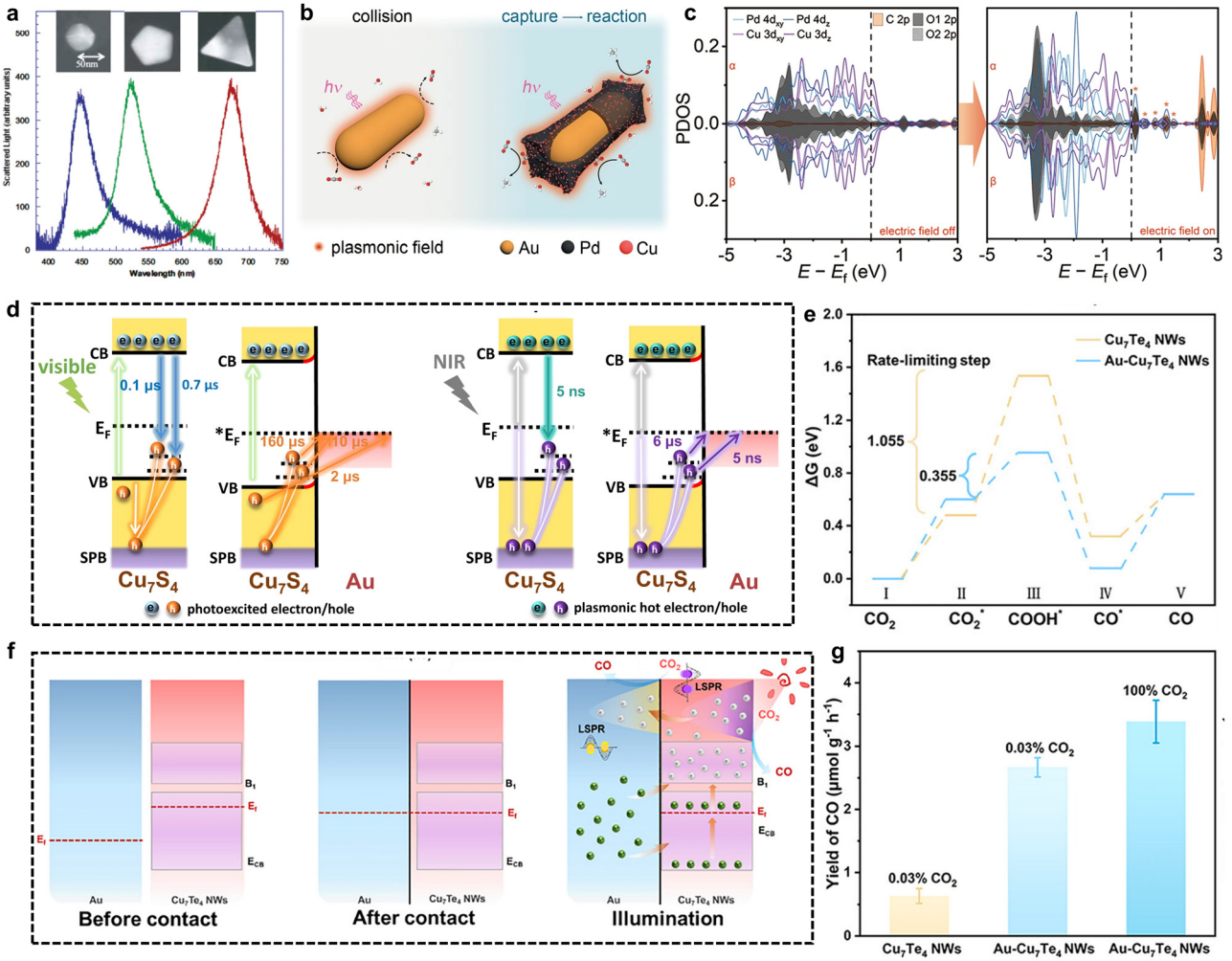

Fig. 6 (a) LSPR of single Ag nanoparticles in different shapes. Reproduced with permission from ref. 147. Copyright 2002, AIP Publishing. (b) Schematic illustration of the role of the CuPd co-catalyst in capturing CO_2 molecules. (c) The projected density of states of CO_2 adsorbed on a CuPd (100) surface in the absence (left) and presence (right) of an electric field pointing toward the surface. The main quasi-isolated trap states are marked with orange asterisks. Reproduced with permission from ref. 91. Copyright 2023, Springer Nature. (d) Proposed mechanism of carrier relaxation pathways for pure Cu_7S_4 and Au@Cu_7S_4 under visible and NIR excitation. Reproduced with permission from ref. 157. Copyright 2024, Springer Nature. (e) Free energy diagrams of CO_2 photoreduction. (f) Schematic of the band configuration and charge transfer at Au–Cu_7Te_4 nanowires for CO_2 photoreduction under IR light illumination. (g) The product formation rate of Cu_7Te_4 and Au–Cu_7Te_4 nanowires for infrared photothermal catalytic CO_2 reduction. Reproduced with permission from ref. 158. Copyright 2025, John Wiley and Sons.

broaden solar utilization, promote reaction kinetics and regulate the reaction path. However, the reaction mechanism of NIR photocatalysis based on the LSPR effect remains a challenge. In particular, the thermal and non-thermal effects are often difficult to decouple and research on the complex excitation and relaxation processes of LSPR is still insufficient, leaving the underlying mechanisms for the enhanced photocatalytic activity unclear. Hot carriers generated by the LSPR effect typically exhibit short lifetimes and are easily influenced by interfacial mass transfer and contact structure, with only a limited fraction remaining that participate in photocatalytic reactions. Additionally, most efficient LSPR-based NIR photocatalysis relies on noble metals, which largely increases the cost and difficulty of large-scale production. In contrast, non-noble metal materials generally show low photocatalytic activity and poor stability. Therefore, future research on NIR photocatalysis based on the LSPR effect should focus not only on developing materials with both low-cost and high activity, but also on photothermal decoupling methods and the underlying reaction mechanisms.

Direct absorption, photon upconversion, and LSPR are the three main strategies for NIR light utilization in NIR photocatalysis. The corresponding materials each have specific advantages and also face different limitations. Direct NIR-responsive materials have the advantage of simple structures and potential for large-scale synthesis. However, their narrow bandgaps often lead to more serious carrier recombination and reduced redox capacity. Upconversion materials can convert NIR light into higher-energy photons to activate wide bandgap photocatalysts, offering good compatibility and flexible design.

Nevertheless, their practical application is constrained by low upconversion efficiency, substantial energy loss, limited material choices, and high cost. LSPR materials usually show strong NIR absorption and photocatalytic performance, owing to the local electric-field enhancement, hot-carrier generation, and photothermal effects. However, the high cost of noble metals, the poor stability of non-noble metal alternatives and the difficulty in separating photonic and thermal contributions still limit their further development. Overall, although clear progress has been made in extending light responses into the NIR region, there is still no universal material strategy that can balance absorption efficiency, photocatalytic activity, stability, and cost. Therefore, future work should pay more attention to combining different strategies in photocatalyst design to achieve efficient, stable, and low-cost NIR photocatalysis.

4. Device design and scale-up considerations for near-infrared light photocatalysis

As research on solar energy utilization advances, NIR photocatalysis has emerged as a promising pathway for harvesting a wider portion of the solar spectrum. In this context, increasing attention is being paid to both the design of efficient photocatalytic systems capable of utilizing NIR light and the standardization of appropriate performance evaluation methods. A comprehensive understanding of device configurations and evaluation parameters is essential to support the rational design, optimization, and application of NIR-driven photocatalytic technologies. The photocatalysts determine the absorption of NIR light, the generation of charge carriers, and the energy conversion pathway, thereby affecting the photocatalytic efficiency. Moreover, devices also have a significant impact on the photocatalytic efficiency by managing the light field, thermal field, and mass transfer processes. To realize efficient NIR-driven photocatalysis, the design and optimization of photocatalytic devices play a crucial role, as they serve as the bridge between photocatalysts and practical applications. Specifically, the uniqueness of NIR light makes it have specific requirements for the optical and thermal management of the device, as well as for its scalability. However, most current research focuses on the development of photocatalysts, while there is little research on the design of the device. Therefore, it is imperative to summarize and discuss the devices for NIR photocatalysis.

4.1. Laboratory-scale reactor configurations

There are diverse laboratory-scale reactor configurations that vary from different classification methods.[159–161] For example, based on the operation mode, they can be classified as continuous, semi-batch, or batch reactors, among which continuous reactors are more suitable for scale-up and engineering applications.[162] In terms of phase contact, there are gas–solid, liquid–solid, and gas–liquid–solid reactors (Fig. 7a–c). The choice of these reactors is usually related to the phase state of the reactants. Gas–solid and liquid–solid reactors are suitable for reactions in which the reactants are only gas or liquid, respectively, while the gas–liquid–solid reactor is used for reactions involving both gaseous and liquid reactants. Compared with liquid–solid reactors, gas–solid reactors offer faster molecular diffusion and more convenient control of gas composition.[163] Although a gas–liquid–solid reactor can utilize both gaseous and liquid reactants, it is constrained by mass transfer at the three-phase interface, and therefore requires more careful interfacial design.[164,165] However, the most typical reactors are slurry and fixed-bed reactors classified by the form of the photocatalyst (Fig. 7d and e). Table 2 presents a comparison of them in terms of merits, limitations and applicable systems.[166–169]

For the slurry reactor, the photocatalyst is dispersed in the liquid phase in the form of powder and maintained in a suspended state through stirring or flow. It is mainly applicable to pollutant degradation, sacrificial agent-assisted HERs, and liquid-phase CO_2RRs. The slurry reactor is the most common reactor configuration in experimental research. It has a simple system, uniform temperature distribution, and is suitable for various materials. However, for NIR photocatalysis, the suspended particles and the liquid limit the penetration of NIR light and the heat utilization. The fixed-bed reactor has the photocatalyst loaded on the surface of a support or filled in the bed, with a fixed light path and reaction interface. It is suitable for gas–solid phase reactions or high-temperature photothermal catalytic reactions, such as gas–solid CO_2RRs and CO_2 hydrogenation reactions. The fixed-bed reactor is conducive to continuous operation and modular design, and is more suitable for practical applications and scale-up. As for NIR photocatalysis, the fixed-bed reactor can better couple the photothermal effect, but poor thermal management makes it more likely to develop local hotspots and spatial temperature gradients, which can lead to the photocatalyst deactivation. Moreover, the photonic and thermal contributions in NIR photocatalysis are difficult to distinguish. Although slurry and fixed-bed reactors remain the most widely employed configurations in laboratory-scale NIR photocatalysis, their limitations have driven the development of new reactor designs to better utilize the unique NIR light, including its deep penetration and photothermal effect. Fluidized-bed reactors have been introduced into photocatalysis because of their uniform temperature distribution, superior heat transfer performance, and enhanced reactant mixing. Ozin investigated the light absorption characteristics of the particles in the photofluidized bed reactor (PFBR) through CFD-DEM simulations and found that PFBR facilitates more uniform contact between reactants, particles, and light, and enhances the utilization of photons.[170] The structure of PFBR is shown in Fig. 7f. Compared to the fixed bed, where light is easily reflected and lost on the bed surface, fluidization increases the particle spacing, allowing light to penetrate deeper into the bed and be absorbed more effectively. In the solar-driven reverse Boudouard reaction experiment, the CO generation rate of the PFBR was 1.6 times higher than that of the fixed bed, and the photon-to-yield

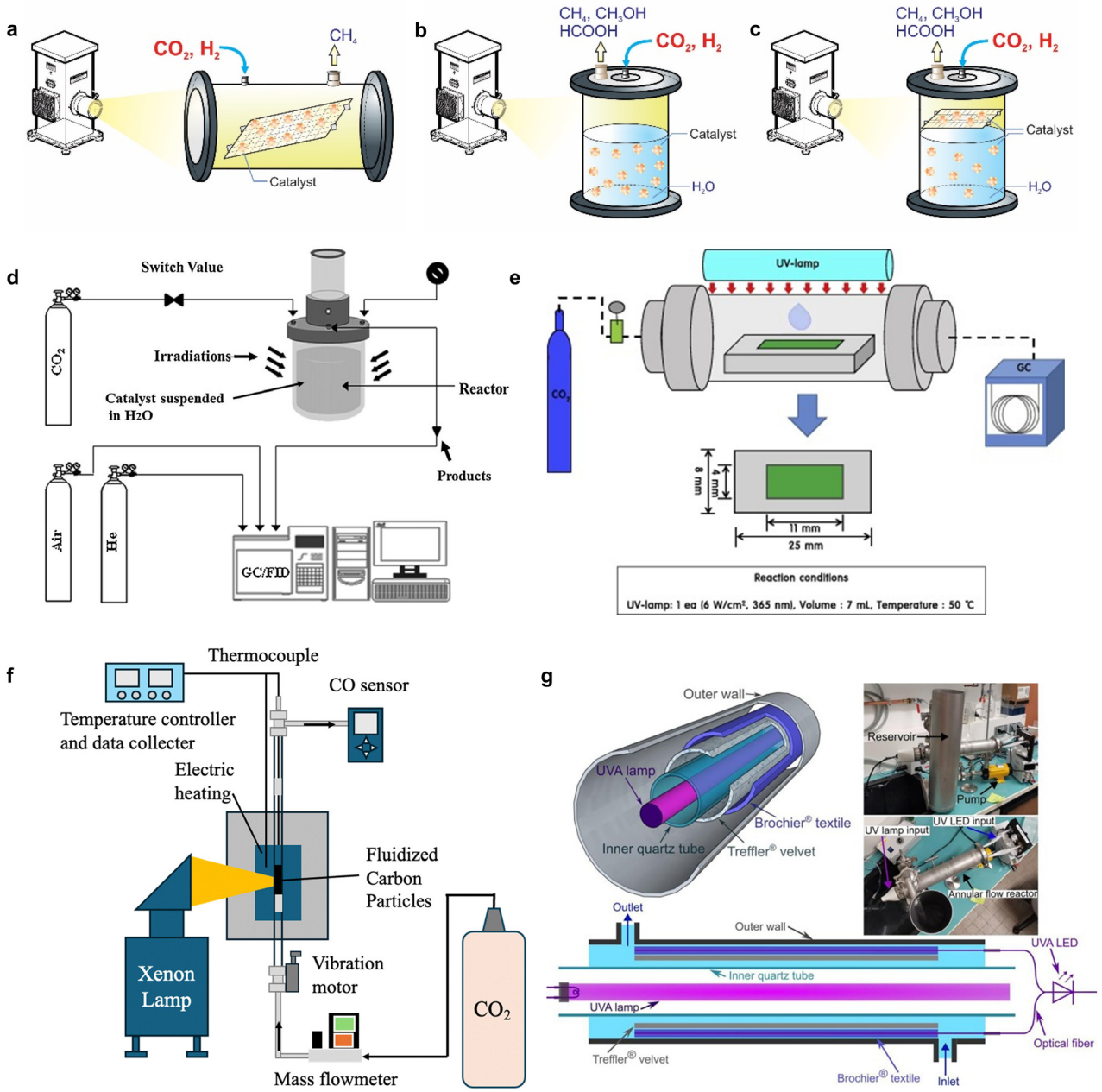

Fig. 7 Three types of reactors with different phase-contact modes: (a) gas–solid reactors, (b) liquid–solid reactors, and (c) gas–liquid–solid reactors. Reproduced with permission from ref. 165. Copyright 2017, Multidisciplinary Digital Publishing Institute. (d) Schematics of a slurry photoreactor. Reproduced with permission from ref. 168. Copyright 2012, Elsevier. (e) Schematic diagram of a fixed-bed reactor for CO_2 photoreduction design with a double-layer film catalyst coated on a glass plate. Reproduced with permission from ref. 169. Copyright 2015, Elsevier. (f) Illustration of the experimental setup of the PFBR. Reproduced with permission from ref. 170. Copyright 2025, The Royal Society of Chemistry. (g) 3D perspective and cross-section side view of the annular flow reactor, along with the real appearance photos (including reservoir and pump parts). Reproduced with permission from ref. 172. Copyright 2025, Elsevier.

efficiency was doubled relative to the fixed bed. The efficient heat and mass transfer, together with the high photon utilization rate of the PFBR, fully meet the design requirements of the NIR photocatalytic reactors. This helps to suppress NIR light-induced local hotspots and efficiently utilize low-energy photons and thermal energy. In addition, Yamamoto *et al.* designed a gap reactor, in which the photocatalyst was confined within a narrow gap between two quartz components.[171] The reduced thickness of the catalytic layer mitigated the temperature gradient induced by incident light, thereby enhancing the conversion and stability of methane dry reforming, while also suppressing side reactions and coke formation.

The light illumination mode also deserves attention. The external illumination systems often suffer from ineffective irradiation, such as scattering and shading. However, the internal illumination systems, which introduce light into the

Table 2 Comparison between three representative reactors across merits, limitations, and applicable systems

Reactor	Merits	Limitations	Applicable systems
Slurry	• Highly exposed photocatalyst area • Good mixing • Large capacity for photocatalyst loading	• Difficult photocatalyst recovery • Poor light penetration under high loading	• Aqueous pollutant degradation • HER • Overall water spilling • Liquid-phase CO_2RR
Fixed-bed	• Good photocatalyst reusability • Compatibility with continuous operation • Highlight penetration • Excellent mass transfer	• Require support material • Large thermal gradient • Photocatalyst detachment	• Continuous water treatment • Gas–solid CO_2RR
Fluidized-bed	• Enhanced light penetration • Strong heat/mass transfer • Good particle–light contact	• Complex hydrodynamics • Difficulties in reactor control	• Gas–solid photocatalysis • Scale-up studies

reactors through optical fibers or light guides, can greatly reduce optical losses. For example, Yan's group has developed an annular flow reactor combined with two side-by-side photocatalytic substrates (Fig. 7g).[172] The inner glass fiber velvet directly received the high-intensity irradiation from the central light source, while the outer self-luminous textile delivered light to the photocatalyst surface through the internal optical fibers. This kind of design achieved synergistic optimization of the light transmission path and catalytic interfaces within a limited reaction volume, thereby enhancing the degradation and mineralization efficiency of pharmaceuticals in real wastewater. However, internally illuminated reactors still face challenges such as non-uniform light-field distribution, light attenuation within the catalytic layer, and high structural complexity. As a result, they remain at an early stage of development, and current studies have been mainly focused on UV or visible light driven pollutant degradation or hydrogen production. For NIR photocatalysis, this type of design suggests that reactor optimization should also consider light-path engineering and spatial arrangement to enhance the effective utilization of low-energy photons.

These different reactor configurations each exhibit distinct advantages and limitations in NIR photocatalysis. Slurry reactors are more suitable for rapid catalyst screening and mechanistic validation, whereas fixed-bed reactors are better suited for continuous operation, stability evaluation, and pre-optimization before scale-up. Meanwhile, photofluidized beds, gap reactors, and annular flow reactors offer new approaches for improving light utilization and intensifying heat and mass transfer, and provide guidance for the design of NIR photocatalytic reactors. Nevertheless, laboratory-scale reactors are still constrained by low photon fluxes and restricted reaction areas, making it difficult to meet the demands of practical application and production. Therefore, a detailed discussion on large-scale NIR photocatalytic devices and system integration strategies is also needed.

4.2. Large-scale devices and system integration

Scaling up laboratory-scale reactors is essential not only for increasing photocatalytic productivity but also as a necessary step toward practical engineering applications. Although direct studies on large-scale NIR photocatalytic devices are still limited, the large-area full-spectrum photocatalytic devices have already made substantial progress. In 2018, Domen's group designed a 1 m^2 flat panel reactor for water splitting, addressing key obstacles to reactor scale-up.[173] By constructing a water layer only 1 mm deep, the evolved H_2 and O_2 bubbles could be rapidly released while maintaining efficient mass transfer. With an illuminated area of 1 m^2, it retained the intrinsic activity of the photocatalyst and achieved an STH efficiency of 0.4% under natural sunlight. In 2021, Domen's group further expanded the flat panel reactor into a 100 m^2-scale photocatalytic panel reactor array, enabling continuous solar water splitting under outdoor conditions for several months, together with the safe separation and collection of the reaction products, as illustrated in Fig. 8a–d.[174] The maximum STH efficiency of the system reached 0.76%. This advancement pushed photocatalytic water splitting from laboratory-scale reactors to a field demonstration at the 100 m^2-scale, indicating that large-scale photocatalysis is already feasible in engineering applications.

Beyond enlarging the illuminated area, the incident photon flux can also be enhanced by integrating solar concentrating devices, thereby improving the utilization of NIR light and even the full solar spectrum. Representative concentrators include parabolic dish concentrators, parabolic trough concentrators, Fresnel lenses, and compound parabolic concentrators (CPC), all of which focus divergent solar radiation onto a smaller area, resulting in a substantial increase in solar energy density.[175–178] Table 3 summarizes the optical principles, concentration ratio, merits and limitations of typical concentrators. Huang *et al.* employed concentrated sunlight to provide heat to drive methane dry reforming.[179] Under simulated solar concentration experiments, the conversion of both CH_4 and CO_2 increased with increasing solar concentration intensity, and the light to chemical conversion efficiency reached as high as 25.9%, while stable operation was maintained for over 800 h. As shown in Fig. 8e, they further developed a dish-engine solar concentrating system with autonomous light tracking capability, enabling efficient solar driven methane dry reforming without any external energy input. Our team also designed a CPC-based reactor (Fig. 8f and g) for solar reforming of

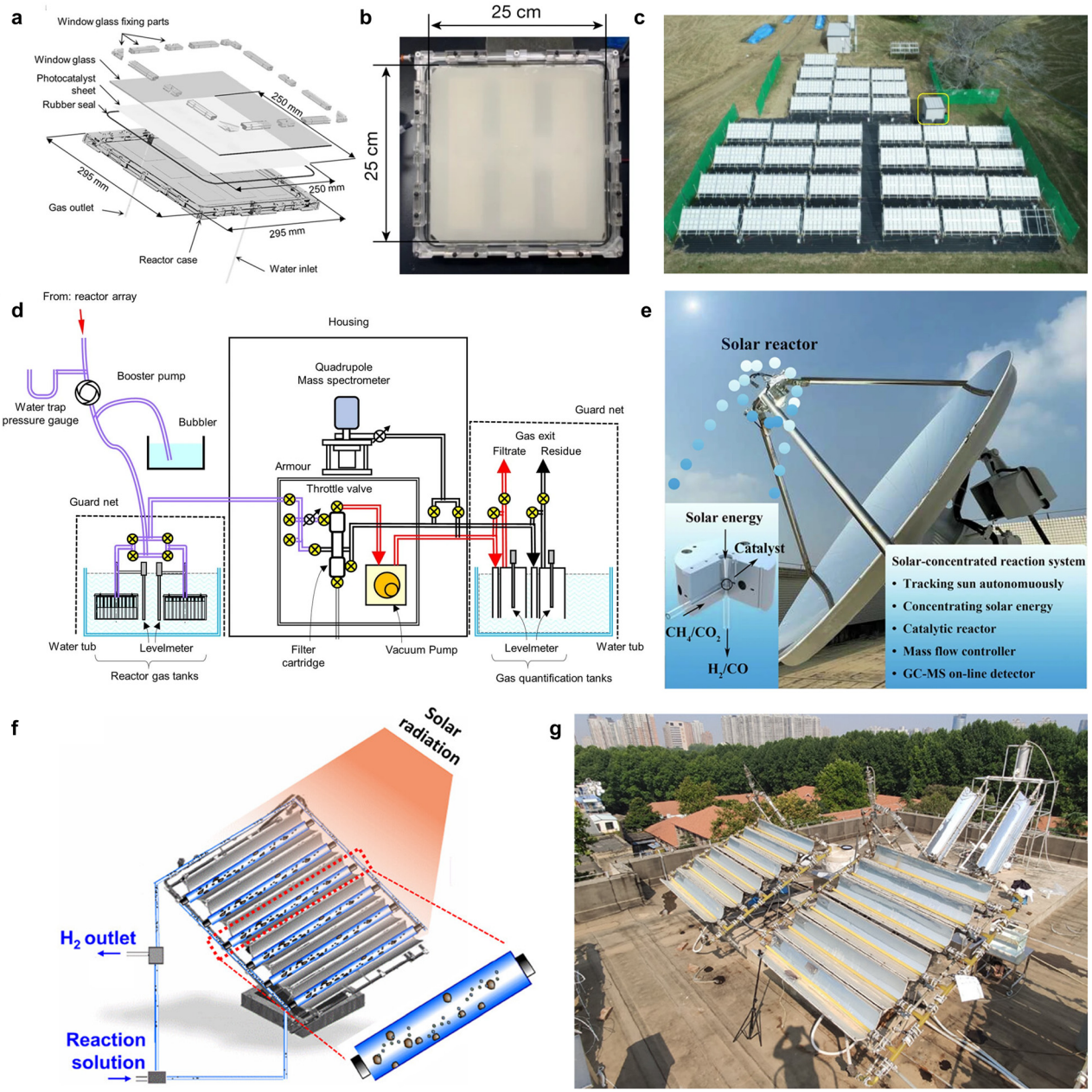

Fig. 8 (a) The design and (b) photograph of a panel reactor unit (625 cm^2). (c) An overhead view of the 100 m^2 solar hydrogen production system with 1600 panel reactor units and a hut housing a gas separation facility (indicated by the yellow box). (d) Schematic of the gas separation apparatus. The routes for the incoming oxyhydrogen gas, hydrogen-enriched filtrate gas and oxygen-enriched residual gas are shown in purple, red and black, respectively. Reproduced with permission from ref. 174. Copyright 2021, Springer Nature. (e) The solar-concentrating catalytic system for methane dry reforming. Reproduced with permission from ref. 179. Copyright 2025, Springer Nature. (f) A CPC device used for water splitting. (g) A photo of the CPC device. Reproduced with permission from ref. 180. Copyright 2023, American Chemical Society.

lignocellulose into H_2 under direct solar light.[180] In this system, previously wasted NIR light is used to increase the reaction temperature, thereby accelerating the photocatalytic process.

In recent years, integrated photocatalytic devices combined with additional functional components have been developed to improve overall energy conversion efficiency, system operability, and application potential under practical conditions. Remo Schäppi *et al.* reported a complete thermochemical solar fuel production process, capturing H_2O and CO_2 directly from the ambient air and directly synthesizing hydrocarbon fuels.[181] Fig. 9a shows the team's solar fuel system, which is divided into three basic units: the direct air capture (DAC) unit, which directly harvests CO_2 and H_2O from the ambient air; the solar redox unit, which converts CO_2 and H_2O into the desired syngas with concentrated solar energy; and gas-to-liquid (GTL) units that convert syngas into liquid hydrocarbons or methanol. Fig. 9b shows a solar redox unit, consisting of a rotatable solar parabolic concentrator that tracks the sun's path to maximize

Table 3 The characteristics of typical concentrators

Concentrator	Optical principles	Concentration ratio	Merits and limitations
Parabolic trough	Line focus	10–100	✓ Mature, scalable ✗ Large, high capital costs, requires sun tracking
Parabolic dish	Point focus	100–2000	✓ High temperature, high photon flux ✗ Hotspot management needed
Fresnel lenses	Point/line focus	10–500	✓ Low cost, lightweight, easy integration ✗ Focal non-uniformity
CPC	Non-imaging focus	1–15	✓ Fixed installation, easy integration ✗ Low concentration ratio

solar energy utilization. Similarly, Reisner integrated a DAC bed with a photocatalytic fixed-bed flow reactor to construct a dual-bed flow reactor for direct air capture and *in situ* photoconversion of CO_2 (Fig. 9c).[182] At night, CO_2 was captured and enriched from air by the solid silica-amine adsorbent in the DAC bed, while during the daytime it was released under the high temperature generated by a parabolic trough solar collector. The released CO_2 was subsequently converted into syngas under illumination over the photocatalyst, thus achieving direct fuel production from air. Photovoltaic and thermoelectric components have also been coupled with photocatalytic devices to promote the efficiency of NIR light utilization and solar energy conversion. Xu *et al.* designed a full spectrum utilization system based on a parabolic trough collector for hydrogen and electricity cogeneration, and a schematic diagram of the hybrid system is illustrated in Fig. 9d.[183] High-energy photons in the solar spectrum are used for photocatalytic water splitting to produce hydrogen, while low-energy photons are collected by the heat collection layer and converted into thermal energy to drive the Rankine cycle for electricity generation. In addition, the dissipated heat and radiant heat loss are recovered and utilized to accelerate the catalytic reaction rate. This system has achieved solar energy conversion efficiencies of 10.34% for chemical energy and 17.85% for electrical energy, respectively, realizing efficient full-spectrum utilization of solar energy.

4.3. Scale-up and engineering considerations for NIR photocatalysis

Compared with visible light, NIR light places more demanding requirements on reactor design. Owing to the low energy of NIR photons and limited utilization efficiency, reactors should be designed to minimize reflection, scattering, and non-productive absorption to maximize the effective use of incident light energy. NIR irradiation is commonly accompanied by significant photothermal effects. Therefore, reactors also require precise temperature field control to prevent performance degradation and poor stability arising from local overheating and uneven temperature distribution. These issues are more prominent in large-scale devices. Simply scaling up a reactor based on geometric similarity cannot adequately account for the nonlinear changes of heat and mass transfer phenomena, often resulting in deteriorated reactor performance. To address this issue, Wang and co-workers developed a photoreactor coupled with a hydrocyclone, where a strong swirling flow enhanced mass transfer in the large-scale photocatalytic system.[184] As a result, the system delivered a hydrogen production rate of 270 mL h^{-1} and an STH efficiency of 5.26%, representing a 4.5-fold improvement over the static case. This study demonstrated that photocatalytic reactor scale-up should not rely solely on geometric enlargement, but must also consider the coupled effects of flow and thermal field, and their impact on the photocatalyst microenvironment.

Following reactor scale-up, system control and operational management also become critical issues. During the scale-up of a wastewater treatment system, Kubiak found that dissolved oxygen depletion limited stable operation.[185]

By integrating real-time monitoring, automated light regulation, and remote sensing, a pilot-scale IoT-controlled real wastewater treatment system was developed, which could actively implement aeration to restore oxidative conditions and improve system operability. This highlights the importance of dynamic control in the operation of large-scale systems. NIR photocatalytic devices also require particular consideration of fluctuations in solar irradiation, which can lead to variations in both light intensity and temperature. Measurement and dynamic regulation of the solar energy input and the temperatures of different device components are therefore essential for maintaining long-term stability and reproducibility. Generally, NIR light appears as thermal energy in photocatalytic systems.

When the generation of NIR photons is significant, local heating and thermal gradients occur on the catalyst particles or catalyst bed, making the accurate temperature mapping within the system difficult. Temperature monitoring should be combined with modeling of heat generation and transport within the photocatalyst. A recent study by Mascaretti *et al.* noted that there is a marked temperature difference between thermocouple measurements and IR sensor measurements, which can lead to differences in the respective roles of pivotal parameters, such as apparent activation energy and heat in the system.[186] Moreover, issues such as the safe collection of products, the compatibility among different modules, cost, and economic analysis also remain important considerations. The efficiency of NIR photocatalysis is not solely determined by the intrinsic properties of the photocatalyst, but is also highly influenced by the reactor and device design.[187] Most studies still rely on conventional laboratory-scale configurations, whereas reactor designs specifically for NIR photocatalysis remain limited. Recent progress has mainly focused on large-area reactor development, coupling with solar concentration technologies, and multi-module system integration, and important advances have already been achieved. A key challenge in NIR reactor design is the simultaneous coordination of effective

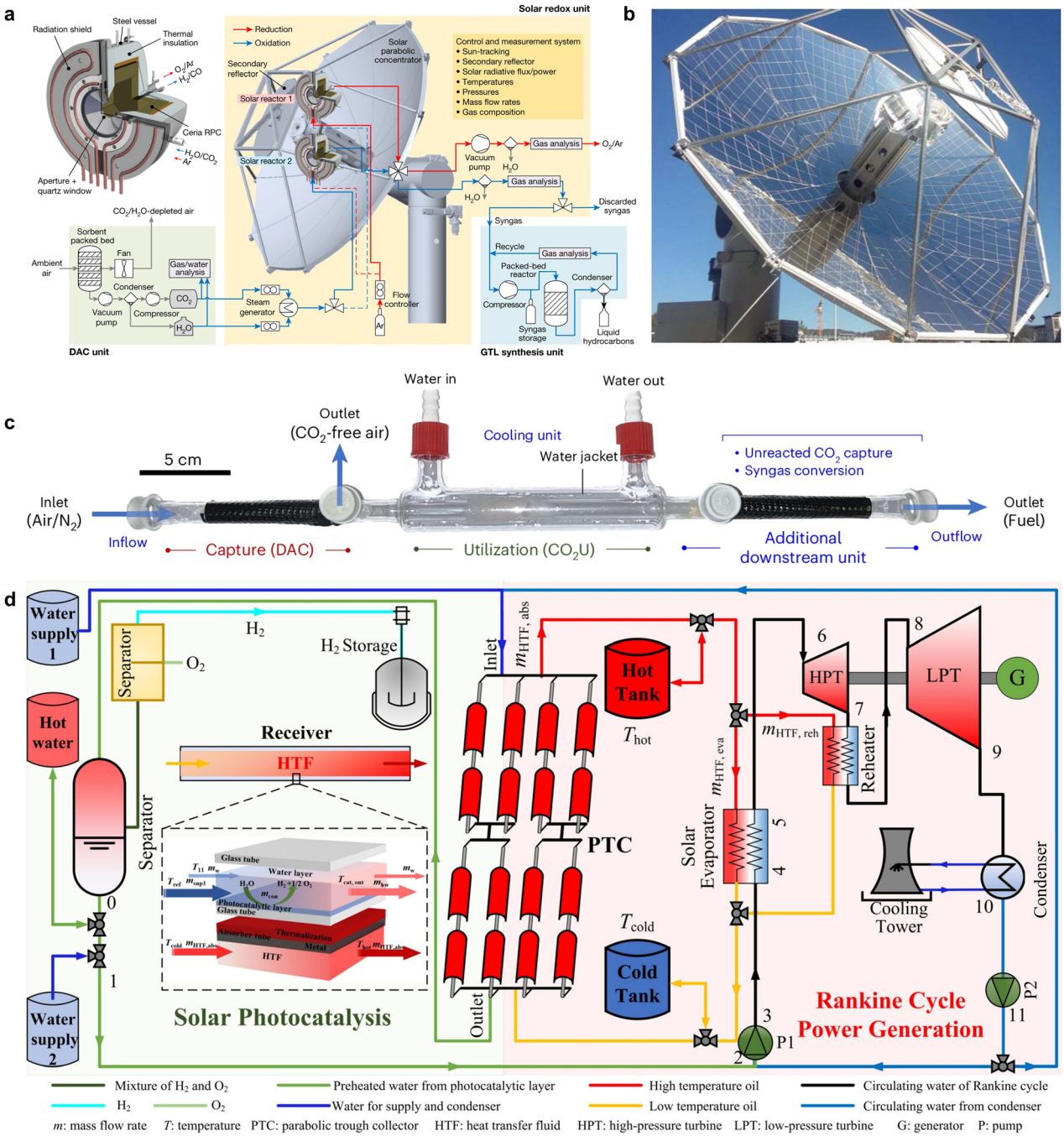

Fig. 9 (a) The solar fuel system consisting of three units: the DAC unit, the solar redox unit, and the gas-to-liquid (GTL) unit. (b) A practical application of the solar-to-fuel technique. Reproduced with permission from ref. 181. Copyright 2021, Springer Nature. (c) Schematics of the designed reactor for in-flow DAC and CO utilization. Reproduced with permission from ref. 182. Copyright 2025, Springer Nature. (d) Schematic diagram of the proposed photocatalysis-thermal power generation hybrid system. Reproduced with permission from ref. 183. Copyright 2025, Elsevier.

low-energy photon input, local temperature distribution, and mass transfer processes. These issues are especially evident in concentrated and integrated systems, where they can strongly affect photocatalytic performance. Accordingly, future device design should place more focus on the synergistic management of light, heat, and mass transfer, together with the matching and control of individual modules, to enable efficient, stable, and durable operation.

5. Performance evaluation in NIR photocatalysis

Although photocatalysis offers an attractive route for converting solar energy into chemical fuels or other valuable products, its practical application is still largely constrained by efficiency. Since efficiency directly determines both the feasibility and economic viability of photocatalytic technologies, it remains a

critical challenge. Notably, NIR light, which constitutes nearly half of the solar spectrum, has the potential to greatly enhance the overall performance of photocatalysis if it can be effectively harnessed. However, the evaluation and definition of NIR photocatalytic efficiency require more rigorous and standardized research.

5.1. Conventional performance evaluation metrics

Photocatalytic performance is usually assessed from multiple aspects, including reaction activity, product distribution, photon utilization efficiency, energy conversion efficiency, and stability. Although the HER, CO_2RR, and pollutant degradation are different reaction systems, their core evaluation metrics can generally be summarized as product rate/removal efficiency, quantum efficiency, solar-to-fuel energy conversion efficiency, and stability.

Production yield is a fundamental metric to measure photocatalytic activity, referring to the quantity of the target product generated by a unit mass of photocatalyst within a unit time (eqn (1)). However, the production yield varies with different light sources or photocatalytic systems and configurations. According to the reported data, the product yield of photocatalytic overall water splitting and the CO_2RR without sacrificial agents is generally in the range of 10–10^2 μmol g^{-1} h^{-1}, while only a few advanced studies exceed 1 mmol g^{-1} h^{-1}.[188–191] With sacrificial agents, the photocatalytic yield usually increases by one to two orders of magnitude, and the HER rate can even reach 10^3 mmol g^{-1} h^{-1}.[192–194] Under concentrated sunlight irradiation, the product yield can be further improved, although it is often normalized by illuminated area rather than photocatalyst mass, which is different from the conventional metric.[195] For example, Ni_1/CeO_{2-x} achieved a CH_4 formation yield of 192.75 μmol cm^{-2} h^{-1} under CO_2 and H_2O vapor conditions.[196] For NIR photocatalysis, production yields are typically lower than those in visible or UV light driven systems.[33,197,198] Recent studies have reported an overall water splitting performance with a H_2/O_2 yield of 1.2/0.6 μmol using a highly crystalline C_3N_4 photocatalyst, and the C_2 hydrocarbon production yield reached 14.2 μmol g^{-1} h^{-1} when driven by NIR light.[103,199]

In photocatalytic pollutant degradation, pollutant removal efficiency is commonly used to quantify the degree of pollutant removal. It is generally defined as the percentage decrease in the amount of the target pollutant relative to its initial value over a given period of time (eqn (2)). Moreover, the degradation rate is reflected by the apparent rate constant (k) (eqn (3)). The larger the k value, the faster the degradation process. The k values reported for pollutant degradation cover a wide range and are typically between 10^{-3} and 10^{-1} min^{-1}.[200,201] Similarly, NIR-driven pollutant degradation typically exhibits lower k values compared to UV/visible photocatalysis.[202,203]

$$Y_{\text{product}} = \frac{\text{Amount of product}}{\text{Irradiation time} \times \text{photocatalyst mass}} \quad (1)$$

$$\eta\ (\%) = \frac{C_0 - C_t}{C_0} \quad (2)$$

$$\ln\left(\frac{C_0}{C_t}\right) = -kt \quad (3)$$

where C_0 represents the initial concentration of the target pollutant, and C_t represents the concentration when the reaction time is t.

For reactions involving multiple products, such as the CO_2RR, product selectivity is also required to describe the product distribution. Product selectivity is typically defined as the proportion of the target product in the total products; a higher selectivity indicates a larger fraction of the desired product (eqn (4)). It is generally related to the reaction mechanism and reflects the photocatalyst's preference for specific intermediates or reaction pathways. Therefore, in multichannel reactions, photocatalytic performance cannot be evaluated solely based on product yield, and an excellent photocatalytic system should exhibit both high activity and selectivity. Taking photocatalytic CO_2RRs as an example, the products of CO_2 reduction are diverse, including C_1 products (CO, CH_4, and HCOOH), C_2 products (C_2H_4, C_2H_6, CH_3COOH, and C_2H_5OH), and even C_3 products. High selectivity toward C_1 products is easier to achieve and has already commonly reached 90%, while some studies have even approached 100%.[204–207] The selectivity toward C_{2+} products is generally lower, usually in the range of 60–80%. However, in recent years, the selectivity for C_2H_4, C_2H_6, and C_2H_5OH has reached 99.1%, 85%, and 98.2%, respectively.[208–211] In NIR photocatalytic CO_2RR systems, the low photon energy generally leads primarily to C_1 species, for which the selectivity can still exceed 90%.[75,212,213] Studies reporting C_2 species as the main products remain limited, and the corresponding selectivity is also lower. In a recent study, the selectivity toward C_2 products was only 63%.[199]

$$S_i\ (\%) = \frac{n_i}{\sum_j n_j} \times 100\% \quad (4)$$

Among them, n_i is the amount of the target product i, and $\sum_j n_j$ is the total amount of all products.

Quantum yield is also an important evaluation metric in photocatalysis, describing the photon utilization efficiency of a photocatalyst. Specifically, the internal quantum efficiency/yield (IQE/IQY) and the apparent quantum efficiency/yield (AQE/AQY) are expressed by eqn (5) and (6). IQE represents the efficiency of effectively converting absorbed photons into excited states or electrons within a material under specific conditions. It reflects the intrinsic properties of the material and takes into account factors such as energy loss and non-radiative recombination. It is an efficiency indicator under ideal conditions and is typically measured under laboratory conditions. AQE takes into account the quantum yield under actual lighting conditions, which is used for performance evaluation in practical research. It depends not only on the intrinsic properties of the material but also on external factors such as the incident angle, spectral distribution, and the reflection and scattering of light. The AQE is generally less than the IQE because not all incident photons are absorbed by

the catalysts. Moreover, the AQE is wavelength-dependent and usually reaches its maximum when the wavelength is close to the absorption edge of the material. In general, the AQE of NIR photocatalysis is lower than that of photocatalysis driven by UV or visible light.

$$\text{IQE/IQY}\ (\%) = \frac{\text{Number of reacted electrons}}{\text{Number of absorbed photons}} \times 100\% \quad (5)$$

$$\text{AQE/AQY}\ (\%) = \frac{\text{Number of reacted electrons}}{\text{Number of incident photons}} \times 100\% \quad (6)$$

According to the reported research, the AQE of overall water splitting is typically in the range of 1–10%, whereas sacrificial agent assisted hydrogen evolution usually shows much higher values.[190,214,215] Representative studies with high quantum efficiency in overall water splitting include the work by Domen's group, where $SrTiO_3$:Al/Rh-Cr_2O_3/CoOOH achieved an AQE of 96% at 350–360 nm (about 100% IQE), and the work by Li's group, where a CdTe QDs/V-In_2S_3 photocatalyst reached an AQE of 73% at 350 nm (with an IQE of 114%).[216,217] In contrast, the quantum efficiency of the photocatalytic CO_2RR is generally much lower, with most reported values remaining below 5%, and only a few studies surpassing 10%.[191,215,218,219] Specifically, the AQE of NIR photocatalysis is usually less than 1%.[110,220,221]

STF/STH is an energy-based metric that quantifies how much solar energy is ultimately converted into chemical energy in H_2 or other fuel products, with stronger universality and comparability. The STF efficiency can be defined as shown in eqn (7). Under one-sun irradiation and without sacrificial agents, the STF efficiency of water splitting is generally below 1% or around 1%, and only a few studies can reach 2–3%.[222–224] The STF of the photocatalytic CO_2RR is still much lower than that of water splitting. For instance, a study on the photocatalytic conversion of CO_2 to formic acid reported an STF of only 0.08%.[225] Although STF values can increase to about 10% for water splitting and about 1% for CO_2RR under concentrated solar light irradiation, direct comparison across studies remains difficult because of the different concentration conditions.[196,226]

$$\eta_{\text{STF}}\ (\%) = \frac{n_{\text{fuel}} \times \Delta G^0}{P_{\text{solar}} \times S \times T} \times 100\% \quad (7)$$

where n_{fuel} (mmol) represents the amount of fuel produced, ΔG^0 (kJ mol^{-1}) is the change in the reaction Gibbs free energy, P_{solar} (mW cm^{-2}) denotes the irradiation intensity, S (cm^2) is the area under light irradiation, and T (s) is the reaction time.

Stability is also a key criterion to evaluate the photocatalytic performance, particularly for large-scale devices. It describes the ability of a photocatalytic system to sustain long-term operation under constant conditions while preserving both photocatalytic activity and material structural stability. However, the stability of photocatalytic systems remains generally limited. In the field of pollutant degradation and CO_2RR, photocatalytic activity is sustained for only 3–5 cycles or dozens of hours. In recent studies, the operating time has been extended to 15 days by optimizing the continuous flow supply of CO_2 and H_2O.[227] In contrast, photocatalytic water splitting typically exhibits longer stability of around 100 h, while highly stable systems can operate for more than 1000 h.[173,174,222] For instance, an Al/Al_2O_3-capped Rh/Cr_2O_3/CoO_x-decorated *p*-InGaN nanowire system for overall water splitting achieved 1500 h of continuous stable operation under concentrated sunlight.[228] Meanwhile, in an earlier study, the $Rh_{2-y}Cr_yO_3$/GaN:ZnO system realized nearly stable overall water splitting for 2160 h while retaining about 50% of its initial activity after 4320 h, representing one of the longest stability records reported in this field.[229] The solar energy conversion efficiency and stability are the two core metrics for the practical application of photocatalysis.

The above metrics and reported performance ranges offer a useful reference for evaluating photocatalytic reactions. However, their applicability is subject to limitations, especially in NIR photocatalysis.

5.2. Limitations of conventional metrics in NIR photocatalysis

The current limitations of NIR photocatalytic performance evaluation mainly lie in two aspects. On the one hand, there are inconsistent experimental and reporting standards. There are various testing conditions used for photocatalytic reactions, making it difficult to compare photocatalytic performance across different studies. Reactor configuration, excitation wavelength, and light intensity will all affect the final product yield. As a result, even the same photocatalyst exhibits different activity under different conditions. Furthermore, sacrificial agents usually lead to higher yield and quantum efficiency, because they can consume electrons or holes more rapidly and replace the slow half reactions, thereby increasing the reaction rate. It has been demonstrated that TEOA can even drive the CO_2RR to produce CH_4 and CO without any other catalyst, under UV light irradiation.[230] In addition, the definitions of some performance metrics are not consistent. For example, the definition of selectivity is ambiguous in some studies, and fails to specify whether it refers to product selectivity or electron selectivity, which further reduces the comparability of reported results.[231,232] In the concentrated photocatalytic system, the definition of illuminated area and light intensity in STF efficiency (eqn (7)) also remains unclear, whether it refers to the area of the light spot or the concentrator, or whether it refers to the intensity before or after concentration.

On the other hand, the unique nature of NIR photons complicates performance evaluation and exposes the limitations of the existing evaluation framework. Performance evaluation of NIR photocatalysis generally relies on the conventional methods employed in traditional photocatalysis, employing parameters such as AQY and STF to assess photon utilization and overall energy conversion. Nevertheless, these metrics exhibit significant limitations in accurately reflecting the mechanisms specific to NIR photocatalysis. Specifically, the calculation of STF only represents the ratio of output chemical energy to input solar energy. However, in NIR photocatalysis, the absorbed photon energy is not solely

utilized for electronic excitation but is also partially dissipated as heat. Consequently, STF fails to distinguish between purely photonic contributions and thermally induced driving forces, which may result in an overestimation of photocatalytic performance.

Similar shortcomings arise in AQY evaluation. Low-energy NIR photons typically require the assistance of auxiliary mechanisms such as thermal effects, LSPR, or nonlinear upconversion to actively participate in photocatalytic reactions. However, the AQY formula is still based on single-photon direct driving, which leads to an overestimation of the effective photon number. As a result, both STF and AQY are unable to capture the synergistic interplay between photonic and thermal processes, nor can they effectively decouple these contributions.

5.3. Recommended reporting standards and evaluation framework

To improve the comparability of results across different studies, it is recommended that each work should report two types of information. One is conventional performance metrics, including product rate or removal efficiency, selectivity, AQY, STF, and stability. These metrics should all be measured and reported, and their calculation methods or equations should be clearly provided. For parameters such as selectivity, which may be defined in different ways, the authors should also explicitly state the specific meaning used in their work, such as product selectivity, electron selectivity, or other forms of selectivity. Another is experimental conditions. At least, key information such as the light source, wavelength range, light intensity, reactor configuration, photocatalyst loading, and reactants should be reported. For non-isothermal systems, temperature monitoring data should also be included. This is especially important in NIR photocatalysis, where irradiation leads to an obvious temperature rise and local hot spots. Therefore, it is necessary to report the photocatalyst surface temperature distribution, the temperature evolution during the reaction, as well as the temperature measurement method and location. In addition, for the calculation of STF in concentrated systems, the irradiation area and light intensity adopted in the calculation should correspond to the same position. It is also recommended to report the type and area of the concentrator, concentration ratio, and the spot area after concentration, allowing for more accurate evaluation and comparison of different concentrated systems.

To address the difficulty of distinguishing photonic and thermal effects in NIR photocatalysis, a series of control experiments should be used to decouple photothermal contributions from pure photocatalytic activity. For instance, compare the reaction results under illuminated and dark conditions at the same temperature, or the performance difference between systems with and without temperature control to provide an initial estimate of the contributions of photonic and thermal effects under NIR irradiation. Furthermore, transient absorption spectroscopy can be employed to monitor the photogenerated carriers and the thermal relaxation process, thereby distinguishing the proportion of photogenerated carriers participating in reactions and those undergoing non-radiative relaxation and forming heat. *In situ* temperature measurement, infrared thermography, or heat transfer simulation can be combined to accurately characterize the temperature distribution and evaluate their impact on photocatalytic performance. In addition, there is still a need to establish quantitative metrics for evaluating photonic effects, thermal effects, and their synergistic interactions.

A single metric is insufficient to describe the true photocatalytic performance, so multiple parameters should be considered together. Under similar reaction conditions, different systems can be compared mainly by product rate, selectivity, and quantum efficiency. For large-scale systems intended for practical application, STF efficiency and stability should also be taken into account, since they better reflect the energy conversion performance and continuous operation capability. In NIR photocatalytic or photothermal catalytic systems, temperature is also an important factor and should be considered together with the catalytic performance. Future directions should therefore focus on establishing unified evaluation protocols for NIR photocatalysis and developing new evaluation metrics that can effectively distinguish between photothermal and photonic effects. A multi-dimensional evaluation framework integrating production yield, AQE, STF, and photothermal conversion efficiency (PCE) would be highly beneficial to provide a more holistic assessment.

6. Conclusion and perspective

As NIR light accounts for a large portion of the solar spectrum, using NIR photons to drive photocatalytic reactions can improve the utilization and conversion efficiency of solar energy. At present, NIR photocatalysis has shown steady progress in the HER, CO_2RR, and pollutant degradation, based on NIR absorption strategies including direct absorption, photon upconversion, and the LSPR effect. At the same time, improving the utilization efficiency of NIR photons through device and system design has also become an important research focus. Nevertheless, the activity and energy conversion efficiency of NIR photocatalysis are still low, and a clear gap remains between current research and practical application. Due to the low energy of NIR photons, although many materials have succeeded in extending light absorption into the NIR region, they still suffer from an insufficient reaction driving force, serious carrier recombination, and limited stability. On the other hand, some high-performance studies still rely on noble metals, rare-earth upconversion materials, or complex preparation methods. This not only increases the cost, but also makes further scale-up more difficult. In addition, many reported results are still based on monochromatic light, short test periods, or the use of sacrificial agents. Truly efficient and stable NIR photocatalytic systems under conditions closer to actual operation are still limited. Addressing these challenges requires further research efforts in the following areas.

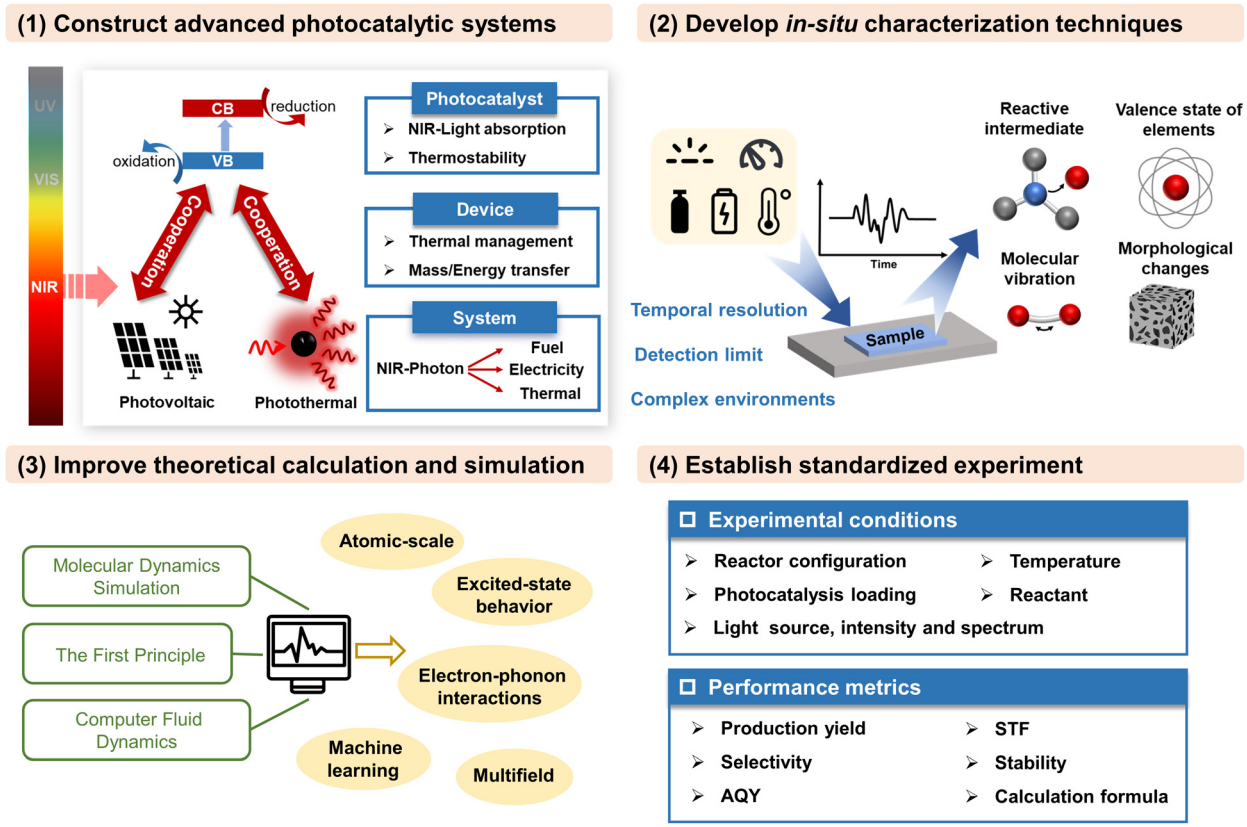

Fig. 10 Outlook for future research in NIR photocatalysis.

6.1. Construct advanced photocatalytic systems

To realize efficient NIR photocatalytic systems, future research should focus on the coordinated optimization of photocatalysts, devices, and systems. The design of NIR-responsive materials should not only extend light absorption but also consider the redox capacity and charge separation efficiency (Fig. 10).

Furthermore, thermal stability is a critical factor, as NIR irradiation and concentrated light inevitably raise system temperatures. Photocatalysts must maintain high-temperature stability to prevent reaction deactivation, and materials such as metal oxides, nitrides, and carbon-based structures offer excellent resistance to thermal degradation. Multiple absorption strategies can also be combined, such as coupling narrow-bandgap semiconductors with LSPR materials or combining photosensitizers with band structure-regulated semiconductors. In terms of device optimization, enhancing thermal management and strengthening mass and energy transfer are crucial to ensure efficient and stable operation under NIR or concentrated light irradiation. Additionally, coupling photocatalytic reactors with photovoltaic or photothermal modules can further broaden solar energy utilization. Meanwhile, the waste heat generated during reactions can be effectively recovered through thermoelectric materials or integrated heat-exchange components, thereby improving overall energy efficiency.

6.2. Develop *in situ* characterization techniques

In situ characterization techniques are usually used for real-time monitoring of the reaction process, which is conducive to an in-depth understanding of the reaction mechanism. However, the unique nature of NIR photocatalytic systems makes *in situ* characterization very difficult. First, the photocatalytic reactions involve ultrafast physical and chemical processes, such as charge carrier generation and recombination, which occur on the picosecond to nanosecond scale. The ultrafast progress exceeds the temporal resolution of some characterization techniques, which makes it hard to observe directly. Second, the coexistence of multiple substances (such as atmosphere, adsorbents, and solvents) in the system will hinder the detection of reaction intermediates and transition species, and also complicate the subsequent data analysis. Additionally, the thermal effects of NIR irradiation can elevate system temperatures, further hindering accurate *in situ* measurements. Overall, complex reaction environments, weak signals, and ultrafast reaction progress greatly hinder the *in situ* characterization of NIR photocatalysis. Therefore, continuous optimization and innovation are needed in experimental design and characterization techniques.

6.3. Improve theoretical calculation and simulation methods

Theoretical calculations can analyze the electronic structure, Fermi levels, adsorption behavior, and reaction energy barriers of photocatalysts at the atomic scale for material screening and mechanistic interpretation. Reactor-scale simulations can model light absorption, scattering, heat distribution, and mass transfer, guiding device optimization and performance

prediction. However, current theoretical and simulation methods still show clear limitations when applied to NIR photocatalysis. Conventional density functional theory focuses on the ground-state structure and fails to describe the excitation, transport and relaxation of photogenerated carriers.[233] Nonadiabatic molecular dynamics can simulate carrier dynamics on the femtosecond to picosecond timescale, but its application is still limited by computational cost, initial-condition sampling, and decoherence treatment.[234,235] In addition, NIR photocatalysis is often accompanied by significant nonradiative relaxation and photothermal effects, whereas existing models still struggle to distinguish the respective roles of photogenerated carriers and heat.[236,237] Future theoretical studies should pay more attention to excited-state behavior after NIR absorption, the role of defect states, interfacial charge transfer, and thermal relaxation processes. Introducing electron–phonon interactions may also help to better describe how nonradiative relaxation is converted into heat.[36] Meanwhile, machine-learning potentials or surrogate models could be combined with multiscale simulations to extend atomistic calculations to larger time and length scales.[238] Strengthening the coupled simulations of optical, thermal, and fluid fields will enable predictions from catalyst design to reactor optimization.

6.4. Establish a standardized experiment

In a photocatalytic system, numerous experimental parameters are involved, such as reaction conditions (temperature, pressure, reactants, atmosphere), light spectrum and intensity, the reactor type (gas–solid or liquid–solid system, flow or fixed-bed system), and the presence of co-catalyst, sacrificial agent, among others. The performance of the catalyst varies significantly under different experimental conditions. In current research, these experimental parameters vary significantly, which greatly reduces the repeatability of experimental results and the comparability among different studies. Furthermore, inconsistencies also exist in the calculation methods used for performance evaluation metrics. For example, the inconsistent reporting of electron selectivity and product selectivity, and the ambiguities in the measurement position of illuminated area and irradiation intensity in the STF calculation. Therefore, it is recommended to establish a standardized reporting framework, including basic performance metrics (production yield, selectivity, AQY, STF, stability) and their corresponding equations, as well as experimental conditions. All of these should be reported in detail to facilitate the comparison of performance across different reaction systems. Additionally, new performance evaluation metrics still need to be established in NIR photocatalysis to decouple and evaluate the contributions of NIR photons and heat to the photocatalytic performance, facilitating the understanding of the underlying NIR photocatalytic mechanisms.

Author contributions

All authors approved the final version of the manuscript. Zhiqing Wang: investigation, data curation, formal analysis, methodology, writing – original draft, writing – review & editing. Fangyuan Wan: investigation, data curation, writing – original draft. Yifei Wang: investigation, formal analysis, writing – original draft. Shengjie Bai: supervision, funding acquisition, project administration. Bin Cao: funding acquisition, resources, software. Feng Wang: supervision, funding acquisition, writing – review & editing, project administration, and conceptualization. Ya Liu: supervision, funding acquisition, resources, validation, writing – review & editing.

Conflicts of interest

There are no conflicts to declare.

Data availability

No primary research results, software or code have been included and no new data were generated or analysed as part of this review.

Acknowledgements

This work is supported by the 2025 Annual Science and Technology Support Project of Daqingshan Laboratory (2025KYPT0188). During the preparation of this work, the authors used the AI tool independently developed by Xi'an Jiaotong University solely in order to improve language and check grammar. After using this tool, the author reviewed and edited the content as needed and take full responsibility for the published article.

References

1 H. Lehtomäki, S. Rao and O. Hänninen, *BMJ*, 2023, **383**, p2774.
2 F. Perera and K. Nadeau, *N. Engl. J. Med.*, 2022, **386**, 2303–2314.
3 J. Lelieveld, K. Klingmüller, A. Pozzer, R. T. Burnett, A. Haines and V. Ramanathan, *Proc. Natl. Acad. Sci. U. S. A.*, 2019, **116**, 7192–7197.
4 A. I. Osman, L. Chen, M. Yang, G. Msigwa, M. Farghali, S. Fawzy, D. W. Rooney and P.-S. Yap, *Environ. Chem. Lett.*, 2023, **21**, 741–764.
5 R. J. Detz, J. N. H. Reek and B. C. C. van der Zwaan, *Energy Environ. Sci.*, 2018, **11**, 1653–1669.
6 Y. Liu, F. Wang, Z. Jiao, S. Bai, H. Qiu and L. Guo, *Electrochem. Energy Rev.*, 2022, **5**, 5.
7 K. Mao, Y. Zhang and S. C. Tan, *Nat. Water*, 2025, **3**, 144–156.
8 R. H. Crabtree, *ACS Energy Lett.*, 2020, **5**, 2505–2507.
9 D. Gunawan, J. Zhang, Q. Li, C. Y. Toe, J. Scott, M. Antonietti, J. Guo and R. Amal, *Adv. Mater.*, 2024, **36**, 1–24.

10 A. Kumar, P. Sharma, G. Sharma, P. Dhiman, G. T. Mola, M. Farghali, A. K. Rashwan, M. Nasr, A. I. Osman and T. Wang, *Environ. Chem. Lett.*, 2024, **22**, 2405–2424.
11 M. J. Molaei, *Fuel*, 2024, **365**, 131–159.
12 Z. Zheng, S. Tian, Y. Feng, S. Zhao, X. Li, S. Wang and Z. He, *Chin. J. Catal.*, 2023, **54**, 88–136.
13 Z. Kuspanov, B. Bakbolat, A. Baimenov, A. Issadykov, M. Yeleuov and C. Daulbayev, *Sci. Total Environ*, 2023, **885**, 1–16.
14 W. Che, S. Zhao, W. J. Byun, T. Tao, J.-P. Jeon, Q. Zhao, Y. Shao, J. Li, J. Kim, J. S. Lee and J.-B. Baek, *Adv. Mater.*, 2025, e06961.
15 X. Li, Y. Chen, Y. Tao, L. Shen, Z. Xu, Z. Bian and H. Li, *Chem. Catal.*, 2022, **2**, 1315–1345.
16 B. Abhishek, A. Jayarama, A. S. Rao, S. S. Nagarkar, A. Dutta, S. P. Duttagupta, S. S. Prabhu and R. Pinto, *Int. J. Hydrogen Energy*, 2024, **81**, 1442–1466.
17 S. B. Beil, S. Bonnet, C. Casadevall, R. J. Detz, F. Eisenreich, S. D. Glover, C. Kerzig, L. Næsborg, S. Pullen, G. Storch, N. Wei and C. Zeymer, *JACS Au*, 2024, **4**, 2746–2766.
18 T. Hisatomi, T. Yamada, H. Nishiyama, T. Takata and K. Domen, *Nat. Rev. Mater.*, 2025, **10**, 769–782.
19 D. C. Cabanero and T. Rovis, *Nat. Rev. Chem.*, 2025, **9**, 28–45.
20 J. Schneider, M. Matsuoka, M. Takeuchi, J. Zhang, Y. Horiuchi, M. Anpo and D. W. Bahnemann, *Chem. Rev.*, 2014, **114**, 9919–9986.
21 Q. Guo, C. Zhou, Z. Ma, Z. Ren, H. Fan and X. Yang, *Annu. Rev. Phys. Chem.*, 2018, **69**, 451–472.
22 Q. Guo, Z. Ma, C. Zhou, Z. Ren and X. Yang, *Chem. Rev.*, 2019, **119**, 11020–11041.
23 K. Nakata and A. Fujishima, *J. Photochem. Photobiol., C*, 2012, **13**, 169–189.
24 S. Y. Tee, J. Kong, J. J. Koh, C. P. Teng, X. Wang, X. Wang, S. L. Teo, W. Thitsartarn, M.-Y. Han and Z. W. Seh, *Nanoscale*, 2024, **16**, 18165–18212.
25 J. Liu, H. Wang and M. Antonietti, *Chem. Soc. Rev.*, 2016, **45**, 2308–2326.
26 J. Liang, X. Yang, Y. Wang, P. He, H. Fu, Y. Zhao, Q. Zou and X. An, *J. Mater. Chem. A*, 2021, **9**, 12898–12922.
27 H. Li, B. Cheng, J. Xu, J. Yu and S. Cao, *EES Catal.*, 2024, **2**, 411–447.
28 X. Cui, Q. Ruan, X. Zhuo, X. Xia, J. Hu, R. Fu, Y. Li, J. Wang and H. Xu, *Chem. Rev.*, 2023, **123**, 6891–6952.
29 C. Han, B. K. Kundu, Y. Liang and Y. Sun, *Adv. Mater.*, 2024, **36**, 1–25.
30 L. Li, X. Han, M. Wang, C. Li, T. Jia and X. Zhao, *Chem. Eng. J.*, 2021, **417**, 1–19.
31 J. Hong, C. Xu, B. Deng, Y. Gao, X. Zhu, X. Zhang and Y. Zhang, *Adv. Sci.*, 2022, **9**, 1–26.
32 W. Li, J. Jing, Z. Wei, J. Xu, W. Shi, H. Wang, X. Zhu, Y. Du, Y. Wang, J. Li and Y. Zhu, *JACS Au*, 2025, **5**, 3500–3512.
33 S. Yang, W. Che, Y. Shao, W. J. Byun, X. Li, X. Jiao, R. Li, J. S. Lee, J. Xu and J.-B. Baek, *Chem. Soc. Rev.*, 2025, **54**, 7174–7215.
34 B. Xie, D. Hu, P. Kumar, V. V. Ordomsky, A. Y. Khodakov and R. Amal, *Joule*, 2024, **8**, 312–333.
35 C. Xu, Q. Tang, W. Tu and L. Wang, *Energy Environ. Sci.*, 2024, **17**, 4461–4480.
36 J. Zhang, H. Chen, X. Duan, H. Sun and S. Wang, *Mater. Today*, 2023, **68**, 234–253.
37 D. Mateo, J. L. Cerrillo, S. Durini and J. Gascon, *Chem. Soc. Rev.*, 2021, **50**, 2173–2210.
38 Y. Lu, H. Zhang, D. Fan, Z. Chen and X. Yang, *J. Hazard. Mater.*, 2022, **423**, 1–18.
39 S. Fang and Y. H. Hu, *Chem. Soc. Rev.*, 2022, **51**, 3609–3647.
40 X. Wu, S. Zhang, S. Ning, C. Yang, L. Li, L. Tang, J. Wang, R. Liu, X. Yin, Y. Zhu, S. Chen and J. Ye, *Chem. Sci.*, 2025, **16**, 4568–4594.
41 X. Wang, A. Rendón-Patiño, D. Mateo and J. Gascon, *EES Catal.*, 2026, DOI: 10.1039/D6EY00013D.
42 B. Su, S. Wang, W. Xing, K. Liu, S.-F. Hung, X. Chen, Y. Fang, G. Zhang, H. Zhang and X. Wang, *Angew. Chem., Int. Ed.*, 2025, **64**, 1–9.
43 C. Pornrungroj, A. B. Mohamad Annuar, Q. Wang, M. Rahaman, S. Bhattacharjee, V. Andrei and E. Reisner, *Nat. Water*, 2023, **1**, 952–960.
44 Z. Wang, C. Cao, L. Jiang, Z. Xing, J. Jia and G. Zhu, *Angew. Chem., Int. Ed.*, 2025, **64**, e202508924.
45 X. Zhang, Y. Jiang, H. Gu, H. Zhang, Y. Li, Z. Lu, S. Zhang, J. Liu, J. Zhang and Z. Tang, *Nat. Commun.*, 2025, **16**, 7612.
46 Y. Wang, P. Maity, Z. Liu, L. Zhao, Y. Li, Z. Fei, X. Pita, N. M. Khashab, H. S. Alqahtani, O. F. Mohammed and H. Zhang, *Adv. Mater.*, 2025, **37**, 2415161.
47 Z. Abou Khalil, A. Nath, K. Hannouche, N. Assaad, G. Mouchaham, A. Beauvois, V. Briois, C. Serre, M. Hmadeh, M. Daturi and M. El-Roz, *Nat. Commun.*, 2025, **17**, 308.
48 C. Han, B. K. Kundu, R. Chen, Pragti, P. Srivastava, C. G. Elles and Y. Sun, *J. Am. Chem. Soc.*, 2025, **147**, 20525–20533.
49 B. Li, Y. Hu, Z. Shen, Z. Ji, L. Yao, S. Zhang, Y. Zou, D. Tang, Y. Qing and S. Wang, *ACS ES&T Eng.*, 2021, **1**, 947–964.
50 Y. Yang, H. Tan, B. Cheng, J. Fan, J. Yu and W. Ho, *Small Methods*, 2021, **5**, 1–46.
51 Y. Cai, F. Luo, Y. Guo, F. Guo, W. Shi and S. Yang, *Molecules*, 2023, **28**, 1–15.
52 F. Zhang, Y.-H. Li, M.-Y. Qi, Y. M. A. Yamada, M. Anpo, Z.-R. Tang and Y.-J. Xu, *Chem. Catal.*, 2021, **1**, 272–297.
53 W. Ye, R. Long, H. Huang and Y. Xiong, *J. Mater. Chem. C*, 2017, **5**, 1008–1021.
54 B. Yang, C. Li, Z. Wang and Q. Dai, *Adv. Mater.*, 2022, **34**, 2107351.
55 A. Sudhaik, A. A. P. Khan, P. Raizada, V.-H. Nguyen, Q. Van Le, A. M. Asiri and P. Singh, *Chemosphere*, 2022, **291**, 132781.
56 X. Chen, Y. Chen, M. Yan and M. Qiu, *ACS Nano*, 2012, **6**, 2550–2557.
57 M. Q. Yang, M. M. Gao, M. H. Hong and G. W. Ho, *Adv. Mater.*, 2018, **30**, 1802894.
58 K. A. Szalkowski Marcin, D. Magdalena, K. Zuzanna, M. Martyna, M. Lukasz, M. Malgorzata, P. Katarzyna, S. Artiom, S. P. James, M. Chan Emory and B. Artur, *Chem. Soc. Rev.*, 2025, **54**, 983–1026.

59 A. Amirjani, N. B. Amlashi and Z. S. Ahmadiani, *ACS Appl. Nano Mater.*, 2023, **6**, 9085–9123.
60 B. Zhou, B. Shi, D. Jin and X. Liu, *Nat. Nanotechnol.*, 2015, **10**, 924–936.
61 M.-F. Joubert, *Opt. Mater.*, 1999, **11**, 181–203.
62 B. S. Richards, D. Hudry, D. Busko, A. Turshatov and I. A. Howard, *Chem. Rev.*, 2021, **121**, 9165–9195.
63 B. K. Kundu, G. Han and Y. Sun, *J. Am. Chem. Soc.*, 2023, **145**, 3535–3542.
64 B. K. Kundu, C. Han, P. Srivastava, S. Nagar, K. E. White, J. A. Krause, C. G. Elles and Y. Sun, *ACS Catal.*, 2023, **13**, 8119–8127.
65 G. Han, G. Li, J. Huang, C. Han, C. Turro and Y. Sun, *Nat. Commun.*, 2022, **13**, 2288.
66 B. Kumar Kundu, N. Bashar, P. Srivastava, C. G. Elles and Y. Sun, *Chem. – Eur. J.*, 2024, **30**, e202402856.
67 G. Wang, B. B. Huang, X. C. Ma, Z. Y. Wang, X. Y. Qin, X. Y. Zhang, Y. Dai and M. H. Whangbo, *Angew. Chem., Int. Ed.*, 2013, **52**, 4810–4813.
68 H. W. Liu, K. Hu, D. F. Yan, R. Chen, Y. Q. Zou, H. B. Liu and S. Y. Wang, *Adv. Mater.*, 2018, **30**, 1800295.
69 M. S. Zhu, Y. Osakada, S. Kim, M. Fujitsuka and T. Majima, *Appl. Catal., B*, 2017, **217**, 285–292.
70 M. Buscema, D. J. Groenendijk, S. I. Blanter, G. A. Steele, H. S. J. van der Zant and A. Castellanos-Gomez, *Nano Lett.*, 2014, **14**, 3347–3352.
71 F. Xu, L. Zheng, J. Zhang, Y. He, H. Cao, X. Zheng, H. García and J. Yu, *Nat. Catal.*, 2026, **9**, 73–86.
72 W. Jiang, Z. M. Wu, X. N. Yue, S. J. Yuan, H. F. Lu and B. Liang, *RSC Adv.*, 2015, **5**, 24064–24071.
73 Y. H. Sang, Z. H. Zhao, M. W. Zhao, P. Hao, Y. H. Leng and H. Liu, *Adv. Mater.*, 2015, **27**, 363–369.
74 G. H. Chen, Y. Q. Yu, K. Zheng, T. Ding, W. L. Wang, Y. Jiang and Q. Yang, *Small*, 2015, **11**, 2848–2855.
75 X. Li, L. Liang, Y. Sun, J. Xu, X. Jiao, X. Xu, H. Ju, Y. Pan, J. Zhu and Y. Xie, *J. Am. Chem. Soc.*, 2019, **141**, 423–430.
76 B. Su, Y. Kong, S. Wang, S. Zuo, W. Lin, Y. Fang, Y. Hou, G. Zhang, H. Zhang and X. Wang, *J. Am. Chem. Soc.*, 2023, **145**, 27415–27423.
77 X. Li, L. Li, G. Chen, X. Chu, X. Liu, C. Naisa, D. Pohl, M. Löffler and X. Feng, *Nat. Commun.*, 2023, **14**, 4034.
78 B. Lin, R. Duan, Y. Li, W. Hua, Y. Zhou, J. Zhou, J. Di, X. Luo, H. Li and W. Zhao, *Adv. Mater.*, 2024, **36**, 2404833.
79 M. Zhu, Y. Osakada, S. Kim, M. Fujitsuka and T. Majima, *Appl. Catal., B*, 2017, **217**, 285–292.
80 B. Zhai, H. Li, G. Gao, Y. Wang, P. Niu, S. Wang and L. Li, *Adv. Funct. Mater.*, 2022, **32**, 2207375.
81 G. Murali, S. P. Vattikuti, Y. K. Kshetri, H. Lee, J. K. R. Modigunta, C. S. Reddy, S. Park, S. Lee, B. Poornaprakash and H. Lee, *Chem. Eng. J.*, 2021, **421**, 129687.
82 S. W. L. Ng, K. J. H. Lim, M. Gao, W. Lu, T. Ghosh, M. Zhang, S. Kawi, M. Hong and G. W. Ho, *Appl. Catal., B*, 2024, **340**, 123182.
83 Y. Li, C. Lou, W. Huang, Z. Ma, S. Lin, X. Xie, T. He, X. Lu, N. Chen and J. Zhuang, *Appl. Catal., B*, 2024, **343**, 123543.
84 W. Xue, H. Sun, X. Hu, X. Bai, J. Fan and E. Liu, *Chin. J. Catal.*, 2022, **43**, 234–245.
85 Y. Lu, X. Jia, Z. Ma, Y. Li, S. Yue, X. Liu and J. Zhang, *Adv. Funct. Mater.*, 2022, **32**, 2203638.
86 X. Cai, L. Mao, S. Yang, K. Han and J. Zhang, *ACS Energy Lett.*, 2018, **3**, 932–939.
87 S. Li, Z. Li, J. Yue, H. Wang, Y. Wang, W. Su, G. I. N. Waterhouse, L. Liu, W. Zhang and Y. Zhao, *Angew. Chem., Int. Ed.*, 2024, **63**, e202407638.
88 K. Q. Hu, Z. W. Huang, X. B. Li, Y. Cheng, X. H. Kong, L. Mei, L. W. Zeng, Z. H. Zhang, J. P. Yu and J. K. Gibson, *Adv. Funct. Mater.*, 2023, **33**, 2213039.
89 C. Sun, J. Yin and H. Fei, *Angew. Chem., Int. Ed.*, 2025, **64**, e202514206.
90 C. Chen, C. Ye, X. Zhao, Y. Zhang, R. Li, Q. Zhang, H. Zhang and Y. Wu, *Nat. Commun.*, 2024, **15**, 7825.
91 C. Hu, X. Chen, J. Low, Y.-W. Yang, H. Li, D. Wu, S. Chen, J. Jin, H. Li, H. Ju, C.-H. Wang, Z. Lu, R. Long, L. Song and Y. Xiong, *Nat. Commun.*, 2023, **14**, 221.
92 J. Li, X. Liu, X. Wu, Z. Liu, Z. Zhao, Y. Liu, S. Dou and Y. Xiao, *Adv. Sci.*, 2024, **11**, 2405668.
93 H. Chen, Y. Xing, S. Liu, J. Fu, H. Shi, Y. Liang, L. Wang and W. Wang, *J. Colloid Interface Sci.*, 2022, **613**, 103–116.
94 K. Wang, Z. Xing, D. Meng, S. Zhang, Z. Li, K. Pan and W. Zhou, *Appl. Catal., B*, 2021, **281**, 119482.
95 Z. Wu, X. Yuan, G. Zeng, L. Jiang, H. Zhong, Y. Xie, H. Wang, X. Chen and H. Wang, *Appl. Catal., B*, 2018, **225**, 8–21.
96 Y. Deng, L. Tang, C. Feng, G. Zeng, J. Wang, Y. Zhou, Y. Liu, B. Peng and H. Feng, *J. Hazard. Mater.*, 2018, **344**, 758–769.
97 H. Li, G. Zhang, C. He, P. Zhang and H. Mi, *ACS Catal.*, 2025, **15**, 15982–15991.
98 Y. Huang, L. Tan, H. Ma, X. Wang, Y. Huang, J. Yin, Z. Liang and X. Luo, *EES Catal.*, 2024, **2**, 675–686.
99 Y. Xu, M. Fan, W. Yang, Y. Xiao, L. Zeng, X. Wu, Q. Xu, C. Su and Q. He, *Adv. Mater.*, 2021, **33**, 2101455.
100 X. B. Chen, L. Liu, P. Y. Yu and S. S. Mao, *Science*, 2011, **331**, 746–750.
101 M. Q. Yang, L. Shen, Y. Lu, S. W. Chee, X. Lu, X. Chi, Z. Chen, Q. H. Xu, U. Mirsaidov and G. W. Ho, *Angew. Chem., Int. Ed.*, 2019, **58**, 3077–3081.
102 J. Li, X. Wu, W. Pan, G. Zhang and H. Chen, *Angew. Chem., Int. Ed.*, 2018, **57**, 491–495.
103 B. Zhai, J. Zeng, Y. Wang, P. Niu, S. Wang and L. Li, *Appl. Catal., B*, 2024, **359**, 124496.
104 Q. Lei, H. Yuan, J. Du, M. Ming, S. Yang, Y. Chen, J. Lei and Z. Han, *Nat. Commun.*, 2023, **14**, 1087.
105 K. Takanabe, K. Kamata, X. Wang, M. Antonietti, J. Kubota and K. Domen, *Phys. Chem. Chem. Phys.*, 2010, **12**, 13020–13025.
106 Y. Chen, C. Jiang, S. Liu, W. Yuan, Q. Li and Z. Li, *Angew. Chem., Int. Ed.*, 2025, **64**, e202419850.
107 X. Zhang, L. Yu, C. Zhuang, T. Peng, R. Li and X. Li, *ACS Catal.*, 2014, **4**, 162–170.
108 X. Zhang, L. Yu, C. Zhuang, T. Peng, R. Li and X. Li, *RSC Adv.*, 2013, **3**, 14363–14370.

109 X. Zhang, T. Peng, L. Yu, R. Li, Q. Li and Z. Li, *ACS Catal.*, 2015, **5**, 504–510.
110 Y. Zhang, C. Pan, G. Bian, J. Xu, Y. Dong, Y. Zhang, Y. Lou, W. Liu and Y. Zhu, *Nat. Energy*, 2023, **8**, 361–371.
111 S. Pascal, S. David, C. Andraud and O. Maury, *Chem. Soc. Rev.*, 2021, **50**, 6613–6658.
112 H. Kumagai, Y. Tamaki and O. Ishitani, *Acc. Chem. Res.*, 2022, **55**, 978–990.
113 D. Kim, V. Q. Dang and T. S. Teets, *Chem. Sci.*, 2024, **15**, 77–94.
114 A. M. May and J. L. Dempsey, *Chem. Sci.*, 2024, **15**, 6661–6678.
115 K.-K. Chen, C.-C. Qin, M.-J. Ding, S. Guo, T.-B. Lu and Z.-M. Zhang, *Proc. Natl. Acad. Sci. U. S. A.*, 2022, **119**, e2213479119.
116 M. H. Elsayed, M. Abdellah, A. Z. Alhakemy, I. M. A. Mekhemer, A. E. A. Aboubakr, B.-H. Chen, A. Sabbah, K.-H. Lin, W.-S. Chiu, S.-J. Lin, C.-Y. Chu, C.-H. Lu, S.-D. Yang, M. G. Mohamed, S.-W. Kuo, C.-H. Hung, L.-C. Chen, K.-H. Chen and H.-H. Chou, *Nat. Commun.*, 2024, **15**, 707.
117 X. Liu, C.-H. Yan and J. A. Capobianco, *Chem. Soc. Rev.*, 2015, **44**, 1299–1301.
118 N. Weitzel, A. Tsutskiridze, J. Bramowski, B. König and T. Hirsch, *Angew. Chem., Int. Ed.*, 2025, **64**, e202511247.
119 Y. Tang, W. Di, X. Zhai, R. Yang and W. Qin, *ACS Catal.*, 2013, **3**, 405–412.
120 Q. Zhang, F. Yang, Z. Xu, M. Chaker and D. Ma, *Nanoscale Horiz.*, 2019, **4**, 579–591.
121 D. W. Zhang Yutong and L. Xinfeng, *Nanoscale*, 2024, **16**, 2747–2764.
122 K. Du, J. Feng, X. Gao and H. Zhang, *Light: Sci. Appl.*, 2022, **11**, 222.
123 T. N. Singh-Rachford and F. N. Castellano, *Coord. Chem. Rev.*, 2010, **254**, 2560–2573.
124 T. F. Schulze and T. W. Schmidt, *Energy Environ. Sci.*, 2015, **8**, 103–125.
125 L. J. Charbonnière, A. M. Nonat, R. C. Knighton and L. Godec, *Chem. Sci.*, 2024, **15**, 3048–3059.
126 M. Ding, C. Lu, Y. Ni and Z. Xu, *Chem. Eng. J.*, 2014, **241**, 477–484.
127 J. B. Zhao, D. Y. Jin, E. P. Schartner, Y. Q. Lu, Y. J. Liu, A. V. Zvyagin, L. X. Zhang, J. M. Dawes, P. Xi, J. A. Piper, E. M. Goldys and T. M. Monro, *Nat. Nanotechnol.*, 2013, **8**, 729–734.
128 X. S. Zhai, S. S. Liu, Y. L. Zhang, G. S. Qin and W. P. Qin, *J. Mater. Chem. C*, 2014, **2**, 2037–2044.
129 W. Gao, B. Tian, W. Zhang, X. Zhang, Y. Wu and G. Lu, *Appl. Catal., B*, 2019, **257**, 117908.
130 X. J. Peng Jie, Z. Wenchao, L. Lin, Y. Dailin, Y. Mi, Z. Pengfei, W. Juan and D. Renren, *Adv. Funct. Mater.*, 2025, **35**, 2422197.
131 D. Jia, X. Li, Q. Chi, J. Low, P. Deng, W. Wu, Y. Wang, K. Zhu, W. Li and M. Xu, *Research*, 2022, 9781453.
132 D. Song, S. Chi, X. Li, C. Wang, Z. Li and Z. Liu, *ACS Appl. Mater. Interfaces*, 2019, **11**, 41100–41108.
133 Y. Ma, Y. Zhang and W. W. Yu, *J. Mater. Chem. C*, 2019, **7**, 13662–13679.
134 H. Li, R. Liu, Y. Liu, H. Huang, H. Yu, H. Ming, S. Lian, S.-T. Lee and Z. Kang, *J. Mater. Chem.*, 2012, **22**, 17470–17475.
135 H. T. Li, X. D. He, Z. H. Kang, H. Huang, Y. Liu, J. L. Liu, S. Y. Lian, C. H. A. Tsang, X. B. Yang and S. T. Lee, *Angew. Chem., Int. Ed.*, 2010, **49**, 4430–4434.
136 X. Zhao, Q. Liu, X. Li, H. Li, Z. Shen, H. Ji and T. Ma, *Angew. Chem.*, 2023, **135**, e202219214.
137 W. Liang, C. Nie, J. Du, Y. Han, G. Zhao, F. Yang, G. Liang and K. Wu, *Nat. Photonics*, 2023, **17**, 346–353.
138 Z. Wang, Z. Yang, R. Fang, Y. Yan, J. Ran and L. Zhang, *Chem. Eng. J.*, 2022, **429**, 132322.
139 X. Zhang, Y. L. Chen, R.-S. Liu and D. P. Tsai, *Rep. Prog. Phys.*, 2013, **76**, 046401.
140 Z. Wang, Z. Yang, Z. C. Kadirova, M. Guo, R. Fang, J. He, Y. Yan and J. Ran, *Coord. Chem. Rev.*, 2022, **473**, 214794.
141 A. Agrawal, S. H. Cho, O. Zandi, S. Ghosh, R. W. Johns and D. J. Milliron, *Chem. Rev.*, 2018, **118**, 3121–3207.
142 J. Zhao, S. Xue, R. Ji, B. Li and J. Li, *Chem. Soc. Rev.*, 2021, **50**, 12070–12097.
143 L. Zhu, M. Gao, C. K. N. Peh and G. W. Ho, *Mater. Horiz.*, 2018, **5**, 323–343.
144 A. Liang, Q. Liu, G. Wen and Z. Jiang, *TrAC, Trends Anal. Chem.*, 2012, **37**, 32–47.
145 V. Amendola, R. Pilot, M. Frasconi, O. M. Maragò and M. A. Iatì, *J. Phys.: Condens. Matter*, 2017, **29**, 203002.
146 E.-S. I. H. Huang Xiaohua, Q. Wei and A. El-Sayed Mostafa, *J. Am. Chem. Soc.*, 2006, **128**, 2115–2120.
147 J. J. B. Mock, M. Smith, D. R. Schultz, D. A. Schultz and S. Schultz, *J. Chem. Phys.*, 2002, **116**, 6755–6759.
148 I. Kriegel, C. Jiang, J. Rodríguez-Fernández, R. D. Schaller, D. V. Talapin, E. da Como and J. Feldmann, *J. Am. Chem. Soc.*, 2012, **134**, 1583–1590.
149 J. M. Luther, P. K. Jain, T. Ewers and A. P. Alivisatos, *Nat. Mater.*, 2011, **10**, 361–366.
150 D. Dorfs, T. Hartling, K. Miszta, N. C. Bigall, M. R. Kim, A. Genovese, A. Falqui, M. Povia and L. Manna, *J. Am. Chem. Soc.*, 2011, **133**, 11175–11180.
151 K. Manthiram and A. P. Alivisatos, *J. Am. Chem. Soc.*, 2012, **134**, 3995–3998.
152 T. M. Mattox, X. Ye, K. Manthiram, P. J. Schuck, A. P. Alivisatos and J. J. Urban, *Adv. Mater.*, 2015, **27**, 5830–5837.
153 Z. Liu, Y. Zhong, I. Shafei, R. Borman, S. Jeong, J. Chen, Y. Losovyj, X. Gao, N. Li, Y. Du, E. Sarnello, T. Li, D. Su, W. Ma and X. Ye, *Nat. Commun.*, 2019, **10**, 1394.
154 M. Sayed, J. Yu, G. Liu and M. Jaroniec, *Chem. Rev.*, 2022, **122**, 10484–10537.
155 Y. F. Zhu, B. Xie, J. A. Yuwono, P. Kumar, A. S. Sharma, M. P. Nielsen, A. Bendavid, R. Amal, J. Scott and E. C. Lovell, *EES Catal.*, 2024, **2**, 834–849.
156 Z. Chen, Y. Yan, K. Sun, L. Tan, F. Guo, X. Du and W. Shi, *J. Colloid Interface Sci.*, 2024, **661**, 12–22.
157 C.-W. Tsao, S. Narra, J.-C. Kao, Y.-C. Lin, C.-Y. Chen, Y.-C. Chin, Z.-J. Huang, W.-H. Huang, C.-C. Huang and C.-W. Luo, *Nat. Commun.*, 2024, **15**, 413.

158 H. Z. Li Mengqian, K. Jie, H. Qinyuan, L. Wenxiu, X. Jiaqi, Y. Wensheng, H. Jun, Z. Junfa, P. Yang, Z. Meng, C. Qingxia and J. Xingchen, *Adv. Mater.*, 2025, 2503021.
159 Y. Li, Y. Ma, K. Li, S. Chen and D. Yue, Photocatalytic Reactor as a Bridge to Link the Commercialization of Photocatalyst in Water and Air Purification, *Catalysts*, 2022, **12**, 724.
160 H. Y. Chung, R. J. Wong, H. Wu, D. Gunawan, R. Amal and Y. H. Ng, *Adv. Energy Mater.*, 2025, **15**, 2404956.
161 V.-H. Nguyen and J. C. S. Wu, *Appl. Catal., A*, 2018, **550**, 122–141.
162 R. Binjhade, R. Mondal and S. Mondal, *J. Environ. Chem. Eng.*, 2022, **10**, 107746.
163 L. Liu, Y. Li, J. He, Q. Wang, J. Deng, X. Chen and C. Yu, *Green Eng. J.*, 2024, **5**, 290–306.
164 X. Ding, W. Liu, J. Zhao, L. Wang and Z. Zou, *Adv. Mater.*, 2025, **37**, 2312093.
165 C.-Y. Chen, J. C. Yu, V.-H. Nguyen, J. C. Wu, W.-H. Wang and K. Kočí, Reactor Design for CO2 Photo-Hydrogenation toward Solar Fuels under Ambient Temperature and Pressure, *Catalysts*, 2017, **7**, 63.
166 A. Manassero, M. L. Satuf and O. M. Alfano, *Chem. Eng. J.*, 2017, **326**, 29–36.
167 K. P. Sundar and S. Kanmani, *Chem. Eng. Res. Des.*, 2020, **154**, 135–150.
168 O. Ola, M. Maroto-Valer, D. Liu, S. Mackintosh, C.-W. Lee and J. C. S. Wu, *Appl. Catal., B*, 2012, **126**, 172–179.
169 M. Park, B. S. Kwak, S. W. Jo and M. Kang, *Energy Convers. Manage.*, 2015, **103**, 431–438.
170 H. Wu, A. Gouda, S. Shan, Z. Zhou and G. Ozin, *EES Catal.*, 2025, **3**, 1246–1256.
171 H. A. El-Naggar, H. Yoshida and A. Yamamoto, *Sustainable Energy Fuels*, 2025, **9**, 1596–1604.
172 Y. Yan, F. Dappozze, C. Prevost, J. Ederer, J. Henych, S. Kříženecká, M. Humble, F. Taulou, L. Peruchon, J.-M. Faurie, S. Parola and C. Guillard, *Chem. Eng. J.*, 2025, **506**, 159951.
173 Y. Goto, T. Hisatomi, Q. Wang, T. Higashi, K. Ishikiriyama, T. Maeda, Y. Sakata, S. Okunaka, H. Tokudome, M. Katayama, S. Akiyama, H. Nishiyama, Y. Inoue, T. Takewaki, T. Setoyama, T. Minegishi, T. Takata, T. Yamada and K. Domen, *Joule*, 2018, **2**, 509–520.
174 H. Nishiyama, T. Yamada, M. Nakabayashi, Y. Maehara, M. Yamaguchi, Y. Kuromiya, Y. Nagatsuma, H. Tokudome, S. Akiyama, T. Watanabe, R. Narushima, S. Okunaka, N. Shibata, T. Takata, T. Hisatomi and K. Domen, *Nature*, 2021, **598**, 304–307.
175 A. Parra-Marfil, G. Blázquez, A. R. Puente-Santiago, B. Weng and M. J. Muñoz-Batista, *Chem. Eng. J.*, 2025, **518**, 164900.
176 W. T. Xie, Y. J. Dai, R. Z. Wang and K. Sumathy, *Renewable Sustainable Energy Rev.*, 2011, **15**, 2588–2606.
177 A. A. Abed, M. R. El-Marghany, W. M. El-Awady and A. M. Hamed, *Sol. Energy Mater. Sol. Cells*, 2024, **273**, 112930.
178 P. D. Tagle-Salazar, K. D. P. Nigam and C. I. Rivera-Solorio, *Green Process. Synth.*, 2020, **9**, 595–649.
179 Z. Rao, Z. Huang, K. Zhang, J. Wang, Y. Feng, K. Wang, Y. Chen, Y. Cao, L. Li, A. Jiang, K. Zheng and Y. Zhou, *Nat. Commun.*, 2025, **16**, 9605.
180 F. Liu, Y. Fu, K. Lu, S. Wang, B. Wang, J. Huang, X. Yan, Y. Zheng, L. Guo and M. Liu, *ACS Catal.*, 2023, **13**, 15591–15602.
181 R. Schäppi, D. Rutz, F. Dähler, A. Muroyama, P. Haueter, J. Lilliestam, A. Patt, P. Furler and A. Steinfeld, *Nature*, 2022, **601**, 63–68.
182 S. Kar, D. Kim, A. Bin Mohamad Annuar, B. B. Sarma, M. Stanton, E. Lam, S. Bhattacharjee, S. Karak, H. F. Greer and E. Reisner, *Nat. Energy*, 2025, **10**, 448–459.
183 E. Zhang, C. Xu, Y. Gao, X. Zhu, Y. Xie, M. Xu and Y. Zhang, *Appl. Energy*, 2025, **377**, 1–15.
184 D. Yang, Y. Yang, F. Zhou, Z. Deng, C. Cui, J. Li, P. Fu, M. Ma, W. Lv, Z. Zhang, X. Yang and H. Wang, *Nat. Commun.*, 2026, **17**, 2170.
185 A. Kubiak, *Chem. Eng. J.*, 2025, **518**, 164709.
186 L. Mascaretti, A. Schirato, T. Montini, A. Alabastri, A. Naldoni and P. Fornasiero, *Joule*, 2022, **6**, 1727–1732.
187 W. K. Fan and M. Tahir, *Chem. Eng. J.*, 2022, **427**, 131617.
188 P. Verma, A. Singh, F. A. Rahimi, P. Sarkar, S. Nath, S. K. Pati and T. K. Maji, *Nat. Commun.*, 2021, **12**, 7313.
189 Z. Cai, H. Liu, J. Dai, B. Li, L. Yang, J. Wang and H. Zhu, *Nat. Commun.*, 2025, **16**, 2601.
190 X. Xin, Y. Li, Y. Zhang, Y. Wang, X. Chi, Y. Wei, C. Diao, J. Su, R. Wang, P. Guo, J. Yu, J. Zhang, A. J. Sobrido, M.-M. Titirici and X. Li, *Nat. Commun.*, 2024, **15**, 337.
191 R. Wang, M. Zhang, J. Liu, X. Wu, S. Zhang, Q. Zhong and J. Yao, *Nat. Commun.*, 2025, **16**, 7844.
192 X. Du, H. Ji, Y. Xu, S. Du, Z. Feng, B. Dong, R. Wang and F. Zhang, *Nat. Commun.*, 2025, **16**, 3024.
193 B. Li, H. Zheng, T. Zhou, Q. Lu, M. Chen, H. Sun, Y. Zhang, Y. Zhang, D. Li, B. Zi, M. Zhang, J. Zhang, J. Zhao, T. He, Z. Zhu, G. Zhang and Q. Liu, *Nat. Commun.*, 2025, **16**, 8276.
194 W. Si, Y. Li, T. Li, H. Liu, Z. Zhang, X. Lu, D. Qiu, Y. Qiao and Y. Lin, *Nat. Commun.*, 2025, **17**, 1052.
195 K.-P. Bai, W.-P. Chen, M.-D. Cui and Y.-Z. Zheng, *Angew. Chem., Int. Ed.*, 2025, **64**, e202511126.
196 Y. Ren, Y. Fu, N. Li, C. You, J. Huang, K. Huang, Z. Sun, J. Zhou, Y. Si, Y. Zhu, W. Chen, L. Duan and M. Liu, *Nat. Commun.*, 2024, **15**, 4675.
197 X. Wu, D. Li, B. Luo, B. Chen, Y. Huang, T. Yu, N. Shen, L. Li and W. Shi, *Appl. Catal., B*, 2023, **325**, 122292.
198 Y. Huang, H. Yang, X. Lu, M. Chen and W. Shi, *Chin. J. Catal.*, 2024, **58**, 105–122.
199 Y. Li, Z. Wang, X. He, C. Sun, Q. Zheng, Y. Jiang, Z. Chen and H. Fei, *Nat. Commun.*, 2026, **17**, 1743.
200 C. Qin, Y. Yang, X. Wu, L. Chen, Z. Liu, L. Tang, L. Lyu, D. Huang, D. Wang, C. Zhang, X. Yuan, W. Liu and H. Wang, *Nat. Commun.*, 2023, **14**, 6740.
201 Y. Hou, P. Zhou, F. Liu, K. Tong, Y. Lu, Z. Li, J. Liang and M. Tong, *Nat. Commun.*, 2024, **15**, 7350.
202 Z. Long, Y. Gao, Y. Zhang, W. Ma, J. Zheng, Y. Liu, F. Ding, Y. Sun and Z. Xu, *RSC Adv.*, 2025, **15**, 764–776.

203 B. Han, S. Yu, D. Zhao, Y. Lou, J. Gao, Z. Liu, Z. Wang and G. Qian, *RSC Adv.*, 2020, **10**, 38798–38804.
204 M. Zhou, Z. Wang, A. Mei, Z. Yang, W. Chen, S. Ou, S. Wang, K. Chen, P. Reiss, K. Qi, J. Ma and Y. Liu, *Nat. Commun.*, 2023, **14**, 2473.
205 C. Chen, M. Wu, Y. Xu, C. Ma, M. Song and G. Jiang, *J. Am. Chem. Soc.*, 2024, **146**, 9163–9171.
206 S. Karmakar, S. Barman, F. A. Rahimi, D. Rambabu, S. Nath and T. K. Maji, *Nat. Commun.*, 2023, **14**, 4508.
207 J. Chen, J. Lu, R. Lang, C. Wang, S. Bao, Y. Li, K. Li and M. Fan, *Green Energy Environ.*, 2025, **10**, 1348–1358.
208 Y. Nie, Y. Li, C. An, X. Tan, Z. Hu, J. Ye and T. Yu, *Appl. Catal., B*, 2024, **345**, 123704.
209 Y. Xiao, G. Ding, J. Tao, Z. Wang, Z. Chen, L. Chen, L. Shuai and G. Liao, *Nat. Commun.*, 2025, **16**, 7476.
210 Z. Tang, Y. Wang, T. Qin, Y. Wei, J. Xiong, X. Wang, X. Li, M. Liu, Y. Liu, X. Liu and Z. Zhao, *Nat. Commun.*, 2026, **17**, 2081.
211 R. Pan, Q. Wang, Y. Zhao, Z. Feng, Y. Xu, Z. Wang, Y. Li, X. Zhang, H. Zhang, J. Liu, X.-K. Gu, J. Zhang, Y. Weng and J. Zhang, *Sci. Adv.*, 2024, **10**, eadq2791.
212 S. Yang, W. J. Byun, F. Zhao, D. Chen, J. Mao, W. Zhang, J. Peng, C. Liu, Y. Pan, J. Hu, J. Zhu, X. Zheng, H. Fu, M. Yuan, H. Chen, R. Li, M. Zhou, W. Che, J.-B. Baek, J. S. Lee and J. Xu, *Adv. Mater.*, 2024, **36**, 2312616.
213 L. Liang, X. Li, J. Zhang, P. Ling, Y. Sun, C. Wang, Q. Zhang, Y. Pan, Q. Xu, J. Zhu, Y. Luo and Y. Xie, *Nano Energy*, 2020, **69**, 104421.
214 K. Bai, X. Yu, G. Wen, Y. Yang, Y. Lin, L. Zhang, J. Rong, L.-C. Yin, W. Qi, M. Bonn, H. I. Wang and G. Liu, *Nat. Commun.*, 2025, **16**, 8577.
215 H. Luo, Z. Liu, H. Lv, J. J. M. Vequizo, M. Zheng, F. Han, Z. Ye, A. Yamakata, W. Shangguan, A. F. Lee, X. Wu, D. Kazunari, J. Lu and Z. Jiang, *Nat. Commun.*, 2025, **16**, 8786.
216 T. Takata, J. Jiang, Y. Sakata, M. Nakabayashi, N. Shibata, V. Nandal, K. Seki, T. Hisatomi and K. Domen, *Nature*, 2020, **581**, 411–414.
217 Y. Zhang, Y. Li, X. Xin, Y. Wang, P. Guo, R. Wang, B. Wang, W. Huang, A. J. Sobrido and X. Li, *Nat. Energy*, 2023, **8**, 504–514.
218 Y. Wang, J.-X. Wei, H.-L. Tang, L.-H. Shao, L.-Z. Dong, X.-Y. Chu, Y.-X. Jiang, G.-L. Zhang, F.-M. Zhang and Y.-Q. Lan, *Nat. Commun.*, 2024, **15**, 8818.
219 W. Lyu, Y. Liu, D. Chen, F. Wang and Y. Li, *Nat. Commun.*, 2024, **15**, 10589.
220 X. Kang, M. Jiang, J. Lv, C. Liao, X. Ding, F. Wang, S. Bai, Y. Liu and L. Guo, *Nat. Commun.*, 2026, **17**, 20260328.
221 H. Ou, Y. Jin, B. Chong, J. Bao, S. Kou, H. Li, Y. Li, X. Yan, B. Lin and G. Yang, *Adv. Mater.*, 2024, **36**, 2404851.
222 L. Lin, Y. Ma, J. J. M. Vequizo, M. Nakabayashi, C. Gu, X. Tao, H. Yoshida, Y. Pihosh, Y. Nishina, A. Yamakata, N. Shibata, T. Hisatomi, T. Takata and K. Domen, *Nat. Commun.*, 2024, **15**, 397.
223 H. Fu, Y. Wu, Y. Guo, T. Sakurai, Q. Zhang, Y. Liu, Z. Zheng, H. Cheng, Z. Wang, B. Huang, Q. Wang, K. Domen and P. Wang, *Nat. Commun.*, 2025, **16**, 990.
224 S. Nandy, T. Hisatomi, T. Takata, T. Setoyama and K. Domen, *J. Mater. Chem. A*, 2023, **11**, 20470–20479.
225 Q. Wang, J. Warnan, S. Rodríguez-Jiménez, J. J. Leung, S. Kalathil, V. Andrei, K. Domen and E. Reisner, *Nat. Energy*, 2020, **5**, 703–710.
226 P. Zhou, I. A. Navid, Y. Ma, Y. Xiao, P. Wang, Z. Ye, B. Zhou, K. Sun and Z. Mi, *Nature*, 2023, **613**, 66–70.
227 H. Jung, H. S. Jeon, M. G. Kim, A. Jamal, I. Gereige, C. Kim and H.-T. Jung, *Nat. Commun.*, 2026, **17**, 70542–70549.
228 I. A. Navid, Z. Ye, Y. Pan, Y. Shen, T. Norris and Z. Mi, *J. Mater. Chem. A*, 2025, **13**, 31642–31653.
229 T. Ohno, L. Bai, T. Hisatomi, K. Maeda and K. Domen, *J. Am. Chem. Soc.*, 2012, **134**, 8254–8259.
230 Z. Liu, J. Li, Z. Chen, M. Li, L. Wang, S. Wu and J. Zhang, *Appl. Catal., B*, 2023, **326**, 122338.
231 M. Bonchio, J. Bonin, O. Ishitani, T.-B. Lu, T. Morikawa, A. J. Morris, E. Reisner, D. Sarkar, F. M. Toma and M. Robert, *Nat. Catal.*, 2023, **6**, 657–665.
232 J. Fu, K. Jiang, X. Qiu, J. Yu and M. Liu, *Mater. Today*, 2020, **32**, 222–243.
233 Ž. Kovačič, B. Likozar and M. Huš, *Chem. Eng. J.*, 2024, **485**, 149894.
234 J. Janoš, P. Slavíček and B. F. E. Curchod, *Acc. Chem. Res.*, 2025, **58**, 261–270.
235 Y. Shu and D. G. Truhlar, *J. Chem. Theory Comput.*, 2023, **19**, 380–395.
236 X. Yu, S. Fan, B. Zhu, S. I. El-Hout, J. Zhang and C. Chen, *Green Energy Environ.*, 2025, **10**, 1377–1436.
237 C. Song, Z. Wang, Z. Yin, D. Xiao and D. Ma, *Chem. Catal.*, 2022, **2**, 52–83.
238 S. Perego and L. Bonati, *npj Comput. Mater.*, 2024, **10**, 291.